

Ataluren Binds to Multiple Protein Synthesis Apparatus Sites and Competitively Inhibits Release Factor Dependent Termination

Shijie Huang

GSK

Arpan Bhattacharya

University of Pennsylvania

Mikel Ghelfi

University of Pennsylvania

Hong Li

University of Pennsylvania

Clark Fritsch

University of Pennsylvania <https://orcid.org/0000-0002-7507-8967>

David Chenoweth

University of Pennsylvania

Yale Goldman

University of Pennsylvania

Barry Cooperman (✉ cooprman@pobox.upenn.edu)

University of Pennsylvania <https://orcid.org/0000-0001-6989-9788>

Article

Keywords:

Posted Date: March 23rd, 2022

DOI: <https://doi.org/10.21203/rs.3.rs-1451662/v1>

License:   This work is licensed under a Creative Commons Attribution 4.0 International License.

[Read Full License](#)

Version of Record: A version of this preprint was published at Nature Communications on May 6th, 2022.
See the published version at <https://doi.org/10.1038/s41467-022-30080-6>.

1 **Ataluren Binds to Multiple Protein Synthesis Apparatus Sites and Competitively Inhibits Release Factor Dependent**
2 **Termination**

3
4
5 Shijie Huang^{1,‡,¥}, Arpan Bhattacharya^{1,2,‡}, Mikel D. Ghelfi¹, Hong Li¹, Clark Fritsch², David M. Chenoweth¹, Yale E.
6 Goldman^{2,#}, and Barry S. Cooperman^{1,#*}
7

8 ¹ Department of Chemistry, University of Pennsylvania, Philadelphia, Pennsylvania 19104, United States

9 ² Department of Physiology, Perelman School of Medicine, University of Pennsylvania, Philadelphia, Pennsylvania 19104,
10 United States

11 [‡] These authors contributed equally: Shijie Huang, Arpan Bhattacharya

12 [#] These authors jointly supervised this work: Yale E. Goldman, Barry S. Cooperman

13 ^{*} To whom to address correspondence. Email: cooprman@upenn.edu

14 [¥] Current address: GSK, 14200 Shady Grove Rd, Rockville, MD 20850
15

16 **ABSTRACT**

17 Genetic diseases are often caused by nonsense mutations, but only one TRID (translation readthrough inducing drug),
18 ataluren, has been approved for clinical use. Ataluren inhibits release factor complex (RFC) termination activity, while not
19 affecting productive binding of near-cognate ternary complex (TC, aa-tRNA.eEF1A.GTP). Here we use photoaffinity
20 labeling to identify two sites of ataluren binding within rRNA, proximal to the decoding center (DC) and the peptidyl transfer
21 center (PTC) of the ribosome, which are directly responsible for ataluren inhibition of termination activity. A third site,
22 within the RFC, has as yet unclear functional consequences. Using single molecule and ensemble fluorescence assays we
23 also demonstrate that termination proceeds via rapid RFC-dependent hydrolysis of peptidyl-tRNA followed by slow release
24 of peptide and tRNA from the ribosome. Ataluren is an apparent competitive inhibitor of productive RFC binding, acting at
25 or before the hydrolysis step. We conclude that designing more potent TRIDs which retain ataluren's low toxicity should
26 target areas of the RFC binding site proximal to the DC and PTC which *do not* overlap the TC binding site.
27

28 INTRODUCTION

29

30 Nonsense mutations, leading to the introduction of a UGA, UAG, or UAA premature stop codon (PSC) within open
31 reading frames, result in premature termination of protein synthesis, giving rise to many human disorders (1, 2). More than
32 11% of known human inherited genetic diseases, including variants of cystic fibrosis, Duchenne muscular dystrophy (DMD),
33 and some forms of cancers are caused by nonsense mutations (3). Several small molecules, denoted translation readthrough
34 inducing drugs (TRIDs) (4), are known to promote at least partial readthrough of PSCs, leading to insertion of an amino acid
35 at the PSC site (5, 6). Currently, the best characterized TRIDs are ataluren (Translarna), a hydrophobic substituted oxadiazole
36 identified as a TRID by PTC Therapeutics Corp., using high throughput screening (7, 8), and the highly polar class of
37 aminoglycoside antibiotics (AGs) (9). As yet, only ataluren has been approved for clinical use. This approval, by the European
38 Medicines Agency, is currently specified for treatment of patients with nonsense-mediated DMD. In addition, ataluren has
39 been shown to be effective in restoring the expression of more than 20 disease-associated genes *in vitro* (10) and *in vivo* (11
40 - 15), and clinical trials are underway for treatment of other diseases (aniridia, NCT02647359; epilepsy, NCT0275826; and
41 colorectal and endometrium cancers, NCT04014530). On the other hand, ataluren has not yet received clinical approval from
42 the US Food and Drug Administration, and, as recently reviewed (6, 16), has been shown to be ineffective in stimulating
43 readthrough in some cellular studies and in achieving favorable outcomes in clinical studies of several other nonsense-
44 mediated diseases. The clinical utility of aminoglycosides has been restricted, in part, by their toxicities (17). Nevertheless,
45 a Phase 2 clinical trial has recently begun (cystic fibrosis, NCT04135495) with a molecularly engineered AG, ELX-02
46 (formerly known as NB124), having much reduced toxicity (18).

47 Efforts to use a rational approach to improve upon the limited clinical success of ataluren have been hampered by the
48 lack of detailed knowledge of both its mechanism of action and its site or sites of interaction with the cell's protein synthesis
49 machinery. Recent cellular studies have provided important details of its relative activities towards the three different stop
50 codons and a determination of which amino acids are inserted into nascent protein chains at PSCs in its presence (19, 20).
51 However, these cell-based assays left unanswered the questions of which specific process or processes within polypeptide
52 elongation or termination does ataluren affect, and where does it interact? To address these questions directly, we have
53 employed a highly purified, eukaryotic cell-free protein synthesis system, denoted PURE-LITE. PURE-LITE is based on the
54 ability of the intergenic internal ribosome entry site (IRES) of Cricket Paralysis Virus (CrPV-IRES) to form a complex with
55 ribosomes capable of initiating polypeptide synthesis in the complete absence of native cytoplasmic initiation factors. In the
56 work described below, PURE-LITE consisted of the following components: 80S ribosomes purified from shrimp cysts,
57 translation factors eEF1A, eEF2, eRF1, and eRF3 from *Saccharomyces cerevisiae*, and aminoacylated tRNAs prepared from
58 *S. cerevisiae* and *Escherichia coli*. As described earlier, despite the heterologous nature of this system, we demonstrated that
59 PURE-LITE could recapitulate some of the effects on readthrough seen in live cell assays of TRIDs, including ataluren, other
60 hydrophobic heterocycles, dubbed ataluren-like, and aminoglycosides (21). This result was not unexpected, given that
61 eukaryotic translation factors have very strongly conserved structures (22 – 24) and charged tRNAs from one species typically
62 form functional complexes with both eEF1A and ribosomes from a different species (25, 26). We have further demonstrated
63 that ataluren and the aminoglycoside G418 (geneticin) stimulate readthrough by orthogonal mechanisms. Ataluren
64 stimulation derives exclusively from its ability to inhibit release factor complex (RFC, eRF1.eRF3.GTP) activity, whereas
65 G418, binding to its high affinity site on the ribosome, increases functional near-cognate tRNA mispairing, with little if any
66 effect on RFC activity (27). The low toxicity of ataluren, in contrast to the much higher toxicity of aminoglycosides which
67 has thus far prevented their clinical use, emphasizes the desirability of developing new TRIDs targeting release factor activity.

68 Here we identify sites of interaction of ataluren within the protein synthesis apparatus by photoaffinity labeling (PAL)
69 experiments utilizing a [³H]-labeled photolabile congener of ataluren, [3-(5-(4-azidophenyl)-1,2,4-oxadiazol-3-yl) benzoic
70 acid], referred to as AzAt throughout the text (Fig. 1a). The targets of the PAL probe are the release factor complex,
71 eRF1.eRF3.GDPNP, in which the non-hydrolyzable analogue GDPNP substitutes for GTP, the Stop-POST5 complex
72 depicted in Fig. 1b, containing FKVRQ-tRNA^{Gln} in the P-site adjacent to the UGA stop codon in the A-site, and the 80S.IRES
73 complex, which lacks FKVRQ-tRNA^{Gln}. Stop-POST5 is an example of a pretermination complex, which we have previously
74 used to characterize ataluren inhibition of RFC-dependent termination (27). Using the PAL approach we identify three sites
75 of ataluren binding within the PURE-LITE system, two within rRNA and one within eRF1. We also use Stop-POST5 as a

76 substrate in the termination reaction, the kinetics of which we examine in detail by single molecule and ensemble approaches
 77 using fluorescent derivatives of FKVRQ-tRNA^{Gln}. These studies demonstrate that ataluren acts as a competitive inhibitor of
 78 RFC through its binding to multiple sites within the protein synthesis apparatus. They further show that tRNA and peptide
 79 release from the ribosome proceed slowly following the much more rapid cleavage of the peptidyl-tRNA bond, and that
 80 ataluren inhibition is exerted only at or before the cleavage step. Both the structural and kinetic results indicate that ataluren
 81 inhibits release factor activity via a cooperative binding mechanism and lead to a suggestion of which areas of the ribosome
 82 could be targeted in the ongoing efforts to develop more effective TRIDs.

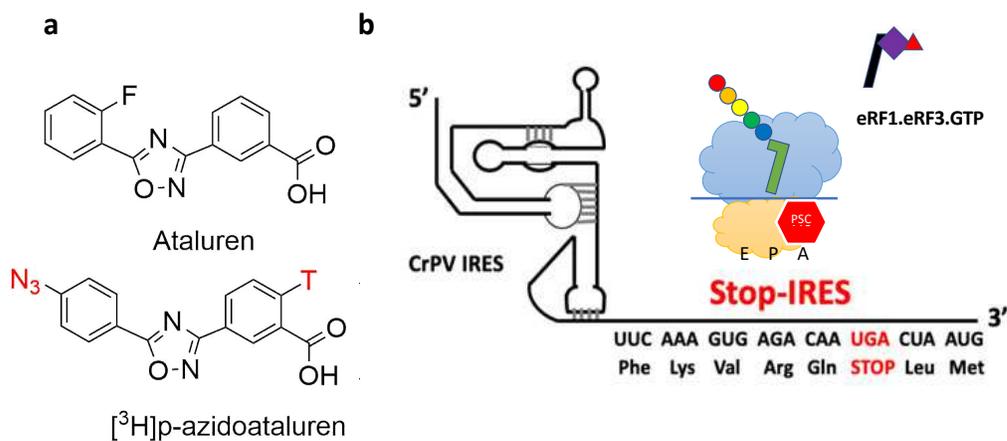


Figure 1. a. Structures of ataluren and [³H]-AzAt. T refers to tritium. N₃ is the azide which confers photolability on azidoataluren. **b.** Stop-IRES mRNA encoding FKVRQStopLM. The cartoon depicts the Stop-POST5 complex containing FKVRQ-tRNA^{Gln} bound in the P-site adjacent to an empty A-site containing the UGA stop codon, and the incoming eRF1.eRF3.GTP complex which catalyzes cleavage of the ester bond linking FKVRQ to tRNA^{Gln} after binding to the A-site.

83

84 RESULTS

85 Photoaffinity Labeling (PAL) Experiments

86 AzAt mimics ataluren in stimulating readthrough of a premature stop codon (Supplementary Fig. 1) and in inhibiting
 87 eRF1/eRF3-catalyzed termination at a premature stop codon (27), showing a lower EC₅₀ than ataluren in both assays.
 88 Photochemical experiments on aryl azides have demonstrated that photolysis of a phenyl azide rapidly forms (in ≤20 ns)
 89 either a ketenimine or azepinone intermediate, which reacts with nucleophiles in approximately 100 μs, increasing the
 90 probability that photoincorporation of photolyzed AzAt will occur in proximity of its binding site. In addition, the reactive
 91 intermediates are rapidly quenched by an amine-containing buffer (28), such as the Tris buffer employed in our studies,
 92 minimizing photoincorporation into a biological target resulting from azide photolysis occurring in solution. We carried out
 93 PAL experiments with [³H]-AzAt in order to identify the binding sites of ataluren within the protein synthesis apparatus of
 94 the PURE-LITE system. We separately performed AzAt-PAL experiments on the Stop-POST5 complex, the 80S.IRES
 95 complex, and eRF1, both alone and within the eRF3.GDPNP ternary complex, giving the photoincorporation (PI) values
 96 shown in Figs. 2a-2c. Here it is important to point out that our preparation of Stop-POST5 had a stoichiometry of 0.40 ± 0.05
 97 PheLysValArgGln-tRNA^{Gln}/ribosome, with the remaining fraction of the ribosome population consisting of the 80S.IRES
 98 complex. As a result, while PI into the 80S.IRES complex and eRF1 could be measured directly, the PI values for the Stop-
 99 POST5 complex are values calculated using eq (1), which corrects for the fraction of 80S.IRES complex present in the Stop-
 100 POST5 preparation. The measured, uncorrected values for the Stop-POST5 complex as a function of AzAt concentration are
 101 shown in Supplementary Fig. 2.

102

$$PI(\text{Stop-POST5})_{\text{corrtd}} = 2.5 \{PI(\text{Stop-POST5})_{\text{measured}} - 0.6 PI(80\text{S.IRES})_{\text{measured}}\} \quad (1)$$

103 Photoincorporation is about 30% higher for Stop-POST5 than for the 80S.IRES complex and, for both targets, most of
104 the photoincorporation ($\geq 70\%$) is found in the RNA fraction, which comprises all six RNA species (26S rRNA, 18S rRNA,
105 5.8S rRNA, 5S rRNA, mRNA, and tRNA) but lacks r-protein. As determined by urea-PAGE analysis (Supplementary Fig.
106 3a) $>90\%$ of the RNA photoincorporation is found within the 18S and 26S rRNA, with the remainder distributed among the
107 smaller RNAs (Supplementary Table 1).

108 We also measured AzAt photoincorporation into either eRF1 or eRF3.GDPNP alone, or into the eRF1.eRF3.GDPNP
109 ternary complex (Fig. 2b). Photoincorporation into isolated eRF1 as a function of AzAt concentration results in a simple
110 hyperbolic saturation curve with an EC_{50} of $110 \pm 20 \mu\text{M}$. The corresponding experiment performed on eRF1 within the
111 eRF1.eRF3.GDPNP ternary complex shows biphasic behavior, consistent with a tight binding site and a much weaker site.
112 The tight site photoincorporation proceeds with an EC_{50} value of $90 \pm 20 \mu\text{M}$, indistinguishable from that found with isolated
113 eRF1. Importantly, both ataluren and GJ072, an ataluren-like TRID (21, 27), substantially inhibit AzAt photoincorporation
114 into isolated eRF1, although the inhibition is less marked within the ternary complex (Fig. 2c). Although AzAt also
115 photoincorporates into isolated eRF3, such photoincorporation is due to either a very weak site binding or to reaction with
116 AzAt photolyzed in solution before binding, since it increases in a strictly linearly fashion up to an AzAt concentration of
117 $500 \mu\text{M}$. Photoincorporation into eRF3 is strongly inhibited within the ternary complex (Supplementary Fig. 4), perhaps due
118 to surface residues in isolated eRF3 becoming buried within the ternary complex.

119 Identifying RNA sites photolabeled by AzAt via nitrene photochemistry

120 The dominance of AzAt photoincorporation into the RNA fraction of both Stop-POST5 and 80S.IRES complexes led us
121 to use LASER-seq (29) to identify the sites of AzAt photoincorporation into RNA. In this method, modified nucleotides
122 show up as point mutations introduced during reverse transcription. We carried out LASER-Seq on four types of samples,
123 denoted PAL, PRE, UV, and NUL. PAL samples were prepared by photoaffinity labeling of complexes with $300 \mu\text{M}$ AzAt,
124 a concentration close to saturating for photoincorporation (Fig. 2a). PRE samples were prepared using separately
125 prephotolyzed AzAt in Buffer 4 (Methods) which was re-irradiated in the presence of complexes. UV and NUL samples were
126 prepared in the absence of AzAt by either subjecting complexes to uv irradiation (UV) or just analyzing complexes directly
127 (NUL).

128 LASER-Seq read coverages were virtually identical for all samples (Supplementary Fig. 5) with, in each case, over 97%
129 of the nucleotides giving at least 10,000 reads. Notable exceptions are tRNA^{Gln}, 26S rRNA 1763-1801 and 18S rRNA 954-
130 956 which gave very low reads, likely due to especially strong secondary structure, and were excluded from downstream
131 analysis. The raw RNA-seq results are presented in Supplementary Data 1. We found very high mutation rates (28% - 100%)
132 in 10 nucleotides in all samples (Supplementary Table 2). Three of these nucleotides have previously been reported to be
133 modified at the conserved sites in *S. cerevisiae* {25S-2870, m⁵C; 18S-1191, m¹acp³Ψ (30); 25S-A645, m¹A (31)} two of
134 which were also reported in human rRNA {28S-A1314, Am; 18S-U1248, m¹acp³Ψ (32)}. To our knowledge, the remaining
135 seven natively modified sites have not been reported previously. In addition, relatively high mutation rates (1.8% - 9.9%)
136 were found in 14 nucleotides in the PAL, PRE, and UV samples (Supplementary Table 3) but not in the NUL samples, and
137 likely include sites of uv-induced crosslinking (33).

138 We first identified the sites of modification arising exclusively via nitrene formation on irradiation of AzAt by the
139 mutation rate fold change of PAL vs. PRE samples, a procedure which corrects for mutation rates arising from either
140 noncovalent binding, covalent photoincorporation of pre-photolyzed AzAt, or uv-induced mutations not related to AzAt
141 (Supplementary Table 3). The results obtained for the $\geq 6,006$ nucleotides present in these two complexes are presented in
142 Supplementary Fig. 6. In examining these data sets to identify potentially interesting sites of AzAt labeling of the Stop-
143 POST5 and 80S.IRES complexes, we initially imposed the constraints that i) the fold-increase (FI) was ≥ 1.5 ; ii) There were
144 ≥ 100 reads for each mutated site; and iii) the results were statistically significant (Z-factor > 0 and p-value < 0.05). These
145 constraints narrowed the number of potentially interesting sites to the 22 identified in Fig. 2d. Strikingly, nucleotide 18S-
146 A1195 has by far the highest fold-increase in both complexes, suggesting that it arises from a site present in both.

147 The large number of nucleotides of potential interest identified in Fig. 2d raised the question of which are most likely to
148 account for ataluren inhibition of release factor activity. To address this question we first used the structure of the fully

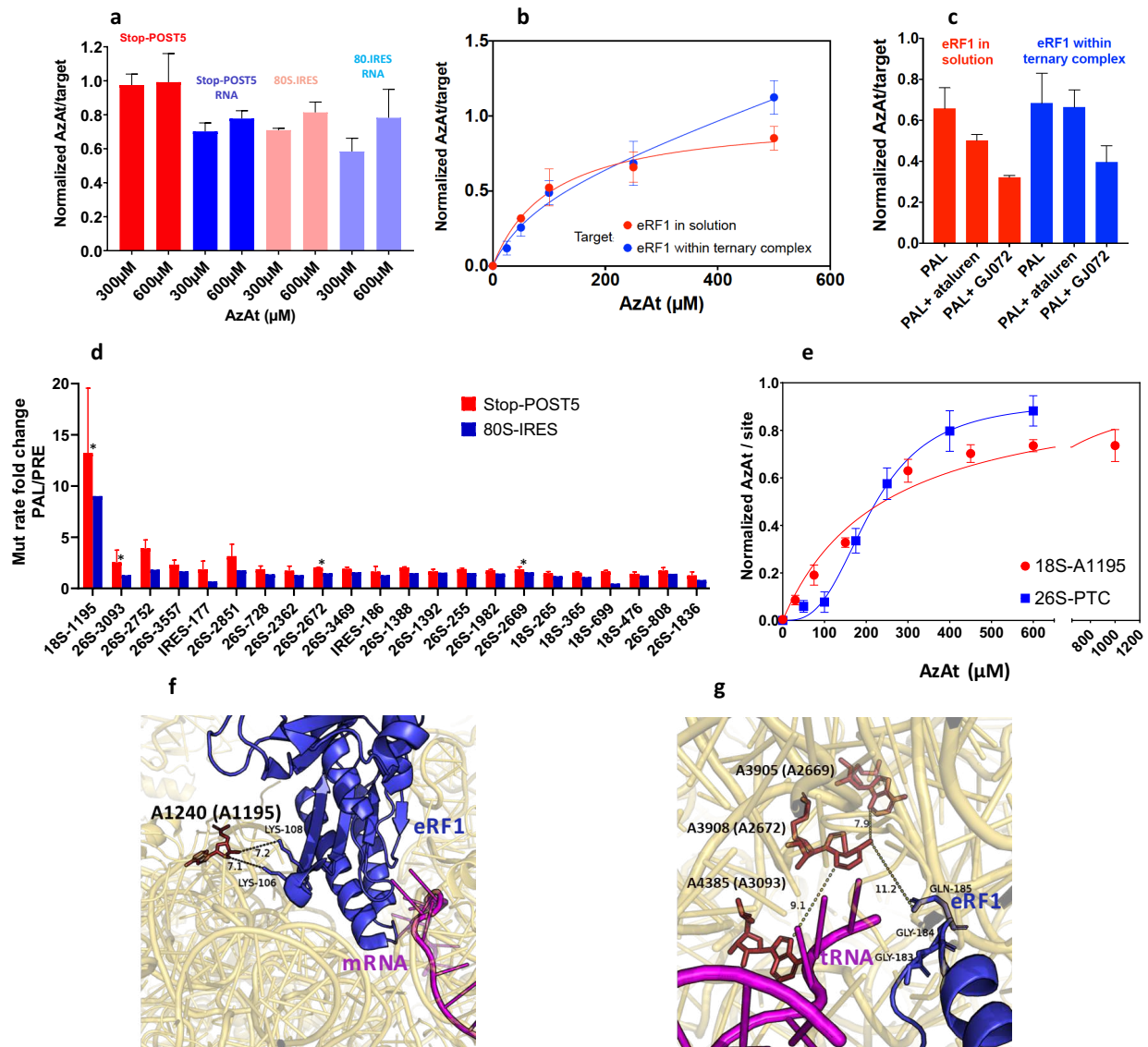


Fig. 2. AzAt Photoaffinity Labeling. **a.** AzAt photoincorporation into Stop-POST5, the RNA fraction of Stop-POST5, 80S.IRES, and the RNA fraction of 80S.IRES. All of the labeling stoichiometries are normalized to that of Stop-POST5 at 600 μM AzAt, which was equal to 1.2/Stop-POST5. **b.** AzAt photoincorporation into eRF1 both alone and complexed with eRF3.GDPNP. The values are normalized to the saturation labeling of isolated eRF1. **c.** Inhibition of AzAt (250 μM) photoincorporation by the addition of either ataluren (1,000 μM) or GJ072 (150 μM). **d.** The mutation rate fold change for PAL vs. PRE samples for Stop-POST5 (red) and 80S.IRES complexes (blue) for the 22 sites most pertinent for ataluren function, and the asterisks indicates sites of particular interest (see text). **e.** Saturation curves for photoincorporation into 18S-A1195, as measured by photoincorporation into Fragment I, vs. the sum of the photoincorporations into 26S A3093, A2669, and A2672, as measured by photoincorporation into Fragments II and III. **f.** Location of A1195 within the 40S subunit containing bound eRF1. **g.** Locations of A2669, A2672, and A3093 within the 60S subunit containing bound eRF1. All of the error bars in this Figure represent average deviations for $n=2$ independent determinations, with the exception of the eRF1 labeling within the ternary complex in **b**, for which $n=3$. Source data for **a – e** are provided as a Source Data file.

149
150

151 accommodated eRF1 bound to a termination complex of the rabbit ribosome (PDB: 5LZU) as a reference to identify
 152 nucleotides labeled by AzAt which are the most proximal to eRF1. Most of the nucleotides in Fig. 2d have distances of closest
 153 approach to eRF1 ≥ 40 Å (Supplementary Fig. 7) and are located at peripheral and flexible loop regions with low evolutionary
 154 conservation among eukaryotic species, suggesting that they are less likely to arise from an AzAt site which interferes with
 155 eRF1 binding. In contrast, three labeled nucleotides, 18S-A1195, 26S-A3093, and 26S-A2672, each fall within 10 Å of eRF1,
 156 and a fourth, 26S-A2669, falls with 16 Å (Supplementary Fig. 7). These four nucleotides, all of which are in highly conserved
 157 and functional regions of rRNA (Supplementary Fig. 8), are indicated with asterisks in Fig. 2d. 18S-A1195 is proximal to the
 158 segment of eRF1 that binds to the termination codon during translation termination (Fig. 2f), is part of the conserved helix
 159 31 loop region, and forms a polar pocket with Tyr123, Lys124, and Lys100 of r-protein uS19 (Supplementary Fig. 9), a
 160 component of the decoding center which is functionally involved in multiple states of translation elongation (34). As shown
 161 in Fig. 2g, 26S-A3093, 26S-A2672 and 26S-A2669 are clustered within the peptidyl transferase center (PTC), in the vicinity
 162 of the catalytically important GGQ motif of eRF1, and extending toward the peptide exit tunnel. In addition, two CrPV-IRES
 163 nucleotides, U177 and G186, have significant fold-increases, and are clustered within the stem loop region of the CrPV-IRES
 164 pseudoknot PKI (Fig S10), which mimics the anti-codon stem loop of the initiator tRNA during translation initiation. As they
 165 are not present in PDB:5LZU it is unclear whether they are proximal to the eRF1 binding site in the POST5 complex, since
 166 it is likely that the CrPV IRES moves away from the tRNA binding sites as the nascent peptide is elongated. Because of this
 167 uncertainty, we included these two nucleotides along with the proximal four mentioned above in our further efforts to identify
 168 functionally important ataluren binding sites.

169 Identifying functionally important sites photolabeled by AzAt

170 We employed an RNase H fragment assay to test which of the six nucleotides selected above correspond to ataluren
 171 binding sites relevant for RFC activity. In this assay, we used oligonucleotide hybridization, RNase H digestion and
 172 polyacrylamide gel electrophoresis (PAGE) to determine the stoichiometry of [³H]-AzAt photoincorporation, measured using
 173 300 μM AzAt, paralleling the LASER-Seq PAL experiments, into the three rRNA fragments and one CrPV fragment that
 174 together include the six nucleotides of potential interest: Fragment I, 18S-A1195; Fragment II, 26S-A3093; Fragment III,
 175 26S-A2669 and 26S-A2672, and Fragment IV, CrPV U177 and G186 (Table 1). In this assay, the background in the PRE
 176 sample is negligible.

Table 1. Photoincorporation yields (mole%) into RNase H Fragments^a						
Target	Experiment	Competing Ligand^b	Mutated site(s)/RNase Fragment			
			18S A1195/ I: 18S 1151 - 1206	26S-A3093/ II: 26S 3069 - 3113	26S- A2669;A2672/ III: 26S 2638 - 2702	CrPV-IRES U177;G186 IV: 156-221
Stop- POST5	PAL, 300 μM AzAt	-	<i>1.55 ± 0.20</i>	0.40 ± 0.01	1.07 ± 0.14	3.2 ± 0.8
		eRF1/eRF3/ GDPNP	0.07 ± 0.03	0.18 ± 0.10	0.19 ± 0.02	2.9 ± 0.6
		eRF1	0.19 ± 0.07	0.18 ± 0.01	0.20 ± 0.01	-
	PAL, 30 μM AzAt	-	0.26 ± 0.03	0.03 ± 0.01	0.13 ± 0.04	-
		Ataluren, 500 μM	0.06 ± 0.01	0.06 ± 0.01	0.10 ± 0.04	-
		GJ072, 150 μM	0.10 ± 0.01	0.07 ± 0.01	0.07 ± 0.01	-
PRE, 300 μM AzAt	-	0.012 ± 0.003	0.04 ± 0.01	0.03 ± 0.02	-	
80S- IRES	PAL, 300 μM AzAt	-	<i>1.03 ± 0.33</i>	<i>0.50 ± 0.09</i>	<i>1.01 ± 0.12</i>	-
		eRF1/eRF3/ GDPNP	0.56 ± 0.06	<i>0.55 ± 0.12</i>	<i>0.94 ± 0.23</i>	-

^a Error ranges are ± average deviations, n=2 or 3 (italicized) independent determinations; ^b Added concentrations: eRF1, 2 μM; eRF3, 4 μM; GDPNP, 1 mM

177 We next asked whether addition of eRF1.eRF3.GDPNP complex inhibits such photoincorporation, consistent with the
178 apparent competitive inhibition of RFC activity by ataluren, as demonstrated below. The results of these experiments,
179 summarized in Table 1, clearly demonstrate that eRF1.eRF3.GDPNP strongly inhibits AzAt photoincorporation into
180 Fragments I – III, while having essentially no effect on photoincorporation into Fragment IV. These results provide a clear
181 suggestion that photoincorporation within Fragments I – III takes place within the eRF1.eRF3.GDPNP binding site, while
182 photoincorporation into Fragment IV does not. As a result, our subsequent experiments focused on determining the effects
183 on AzAt photoincorporation into Fragments I – III of various modifications in experimental protocol. Further
184 photoincorporation results into Fragment IV, and for several other RNA sites showing somewhat high AzAt
185 photoincorporations but which were not strongly inhibited by eRF1.eRF3.GDPNP, are presented in Supplementary
186 Information (Supplementary Table 1 and Supplementary Notes).

187 Somewhat surprisingly in view of published cryoEM structures (35), added eRF1 alone has very similar effects on
188 photoincorporation into Fragments I - III as the eRF1.eRF3.GDPNP complex, a point we return to in the Discussion.
189 Photoincorporation into Fragments I - III derived from 80S.IRES is roughly similar to what we find for Stop-POST5, but the
190 effects of added eRF1.eRF3.GDPNP complex are quite different, with no measured inhibition of photoincorporation into
191 Fragments II and III and only partial inhibition of photoincorporation into Fragment I. These results reflect the expected
192 weaker binding of the RFC to the ribosome in the absence of a stop codon at the A-site, and also imply that such weaker
193 binding is not accompanied by a conformational change that results in eRF1 interaction with the PTC.

194 Next we determined whether added ataluren or the ataluren-like TRID GJ072 inhibited AzAt photoincorporation into
195 Fragments I – III (Table 1) of the Stop-POST5 complex. These experiments were performed at a much lower AzAt
196 concentration than those mentioned above (30 μ M vs. 300 μ M), because we expected that inhibition would be incomplete at
197 high AzAt concentration, based on the relative EC_{50} values of ataluren > AzAt \approx GJ072 as termination inhibitors (27) and the
198 limited solubility of GJ072 in aqueous medium. Photoincorporation into Fragment I, reflecting 18S A1195 labeling, is
199 strongly inhibited by ataluren and GJ072. Taken together with the proximity of 18S A1195 to a region of eRF1 that interacts
200 with mRNA in the decoding center of the small subunit (Fig. 2f), the results in Table 1 provide strong evidence that 18S
201 A1195 is labeled from a functionally important ataluren binding site which inhibits both eRF1.eRF3.GDPNP and eRF1
202 binding. However, photoincorporation into Fragment III, reflecting A2669/A2672 photolabeling, is only weakly inhibited by
203 ataluren and GJ072, and photoincorporation into Fragment II, reflecting A3093 photolabeling, is actually stimulated. These
204 results could indicate that photolabeling of the PTC sites does not proceed from a true ataluren binding site, but an alternative
205 interpretation is that the results arise from two opposite effects: a direct competition by ataluren and GJ072 with AzAt at the
206 PTC and an allosteric stimulation of AzAt binding at the PTC by ataluren or GJ072 binding elsewhere within the ribosome.
207 To resolve this uncertainty we determined the AzAt concentration dependence of photoincorporation into these PTC sites
208 (Fragments II and III) and into A1195 (Fragment I). We found that photoincorporation into Fragment I can be fit to a simple
209 hyperbolic binding isotherm with an EC_{50} of $240 \pm 10 \mu$ M (Fig. 2e), but that photoincorporation into Fragments II and III
210 both show clear evidence of cooperativity, with saturation curves which are quite similar to one another (Supplementary Fig.
211 11). This latter result, and the mutual proximities of 26S-A3093, 28S-A2672, and 28S-2669 (Fig. 2g), suggest that
212 photoincorporation into these three nucleotides occurs from a single binding site within the PTC. Accordingly, in Fig. 2e we
213 compare the normalized values of the combined saturation curve for Fragments II and III with the normalized values for the
214 saturation curve of Fragment I, showing the clear difference in the shape of the curves. Fitting the saturation curve for
215 Fragments II and III to eq (2) yielded a K_A equal to $200 \pm 40 \mu$ M and a Hill n of 3.0 ± 0.3 .

216
$$PI = \frac{PI_{max}[AzAt]^n}{(K_A^n + [AzAt]^n)} \quad (2)$$

217 **Ataluren is an apparent competitive inhibitor of RFC-dependent termination of polypeptide synthesis**

218 We used two different fluorescent assays to quantify ataluren inhibition of termination. As described in Table 2, smTIRF
219 assays employed three doubly-labeled forms of the Stop-POST5 complex, Atto(pep)-Cy(tRNA)-Stop-POST5, Atto(rbsm)-
220 Cy(tRNA)-Stop-POST5, and Atto(pep)-Cy(rbsm)-Stop-POST5. Ensemble fluorescence anisotropy studies employed the
221 singly-labeled form, Atto(pep)-Stop-POST5. In Atto(pep)-Stop-POST5, Atto(pep)-Cy(tRNA)-Stop-POST5, and Atto(pep)-
222 Cy(rbsm)-Stop-POST5, the lysine epsilon amino group in the pentapeptide is derivatized with Atto-647. In Atto(pep)-

223 Cy(tRNA)-Stop-POST5 and Atto(rbsm)-Cy(tRNA)-Stop-POST5, a dihydrouridine residue of tRNA^{Gln} is derivatized with
 224 Cy3. In Atto(rbsm)-Cy(tRNA)-Stop-POST5, the ribosome is labeled with Atto-647N. In Atto(pep)-Cy(rbsm)-Stop-POST5,
 225 the ribosome is labeled with Cy3.

Stop-POST5	Lys within FKVRN	tRNA ^{Gln}	Ribosome ^a
Atto(pep)	Atto647	unlabeled	unlabeled
Atto(pep)-Cy(tRNA)	Atto647	Cy3	unlabeled
Atto(rbsm)-Cy(tRNA)	unlabeled	Cy3	Atto647N
Atto(pep)-Cy(rbsm)	Atto647	unlabeled	Cy3

^a ribosomes were labeled to a total stoichiometry of ~ 1/ribosome spread over Lys residues within r-proteins

226
 227 **smTIRF results using Atto(pep)-Cy(tRNA)-Stop-POST5 attached to surface-immobilized ribosomes**

228 Although the distance between the two fluorophores is not close enough to produce FRET, fluorescent pairs could be
 229 identified by co-localization on the slide under alternating 532 nm and 640 nm TIRF illumination. This permits near-
 230 simultaneous monitoring of the dynamics of peptide and P-site tRNA release from the Stop-POST5 complex following RFC
 231 binding. To reduce photobleaching of each fluorophore, we recorded time-lapse movies, with bursts of 20 or 50 frames at
 232 100 ms frame intervals interleaved by 20 s intervals with the lasers shuttered. Total recording time for each trial was 20 min.
 233 Figs. 3a,c show typical frame by frame recordings indicating a loss of signal for both labeled peptide and labeled tRNA after

234 the addition of the RFC to
 235 Atto(pep)-Cy(tRNA)-Stop-
 236 POST5. The corresponding
 237 results plotted in actual time
 238 are shown in Figs. 3b,d. Either
 239 peptide (a) or tRNA (b) can
 240 dissociate first, in
 241 approximately equal
 242 proportions. Photobleaching
 243 of Cy3-labeled tRNA and
 244 Atto647-labeled peptide in the
 245 absence of eRF1/eRF3 was
 246 much slower (Figs. 3e,f).
 247 Under the time lapse
 248 illumination employed, mean
 249 lifetimes for Atto647-peptide
 250 and Cy3-tRNA at 0.32 μ M
 251 eRF1 and 2 μ M eRF3 were
 252 each 2.45 min. By
 253 comparison, in the absence of
 254 RFC, the mean lifetimes under
 255 time-lapse illumination before
 256 Atto647 and Cy3
 257 disappearance were 6.8 min
 258 and 4.9 min, respectively,
 259 which were mainly due to
 260 photobleaching. Since the

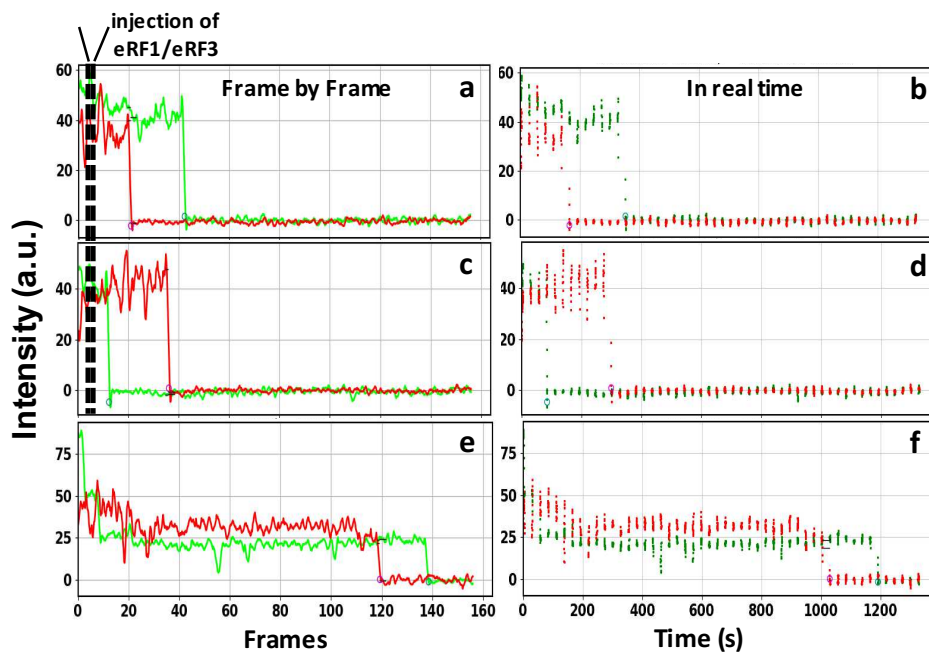


Figure 3. Typical traces showing the dissociation of Atto-647 labeled peptide (red) and Cy3-labeled tRNA (green) following eRF1/eRF3 injection. In the time-lapse experiment the sample was briefly illuminated between fixed time intervals. **a.** and **c.** Sample traces following eRF1/eRF3 injection. In **a** the peptide signal disappears prior to tRNA signal; in **c** the tRNA signal disappears prior to peptide signal. **b.** and **d.** Corresponding real-time scatter plots of the traces presented in **a** and **c**, where each dot represents one frame. **e.** Sample trace from a control experiment where only buffer was injected to obtain the photobleaching/spontaneous dissociation rate, which is clearly much slower than the rates seen in **a** and **c**. **f.** The real-time scatter plot of the trace presented in **e**.

261 single-step decrease of fluorescence intensity is due either to photobleaching or to dissociation of peptide or tRNA from the
262 ribosome, we calculate the RFC-dependent rate constant for peptide or tRNA dissociation, k_{RF} , as equal to $1/\langle T_{obs} \rangle - 1/\langle T_{pb} \rangle$,
263 where $\langle T_{obs} \rangle$ is the mean observed lifetime and $\langle T_{pb} \rangle$ is the mean time until signal loss in the absence of RFs.

264 We next determined k_{RF} values for peptide and tRNA dissociation as a function of both RFC and ataluren concentrations.
265 Figs. 4a,b shows examples of cumulative distributions of peptide and tRNA dissociation times at 320 nM RFC, 32 nM RFC,
266 and 32 nM RFC plus 1 mM ataluren. Fitting these results to single exponentials and subtracting the photobleaching rate gave
267 average k_{RF} values. In the absence of ataluren, values of k_{RF} as a function of RFC concentration fit well to the Michaelis-
268 Menten equation, yielding values of $V_{max} = \sim 0.27 \pm 0.02 \text{ min}^{-1}$ peptide and $0.20 \pm 0.02 \text{ min}^{-1}$ for peptide and tRNA
269 dissociation, respectively, and an $EC_{50} = \sim 0.02 \text{ }\mu\text{M}$ for each (Figs. 4c,d, red curves). Addition of ataluren at concentrations
270 of 200, 500, and 1000 μM (Figs. 4c,d) raised EC_{50} values significantly, reaching $\sim 0.1 \text{ }\mu\text{M}$ at 1000 μM , whereas V_{max} values
271 at high RFC concentration were little affected, a strong indication that ataluren acts as an apparent competitive inhibitor of
272 RFC. Separate control experiments performed in the absence of ataluren with Atto(rbsm)-Cy(tRNA)-Stop-POST5 and
273 Atto(pep)-Cy(rbsm)-Stop-POST5 at a saturating concentration of RFC (0.65 μM eRF1, 1.3 μM eRF3) gave rate constants,
274 $0.20 \pm 0.03 \text{ min}^{-1}$ and $0.26 \pm 0.03 \text{ min}^{-1}$ for tRNA and peptide dissociation, respectively, indistinguishable from those
275 measured for Atto(pep)-Cy(tRNA)-Stop-POST5, showing that labeled peptide did not inhibit tRNA dissociation and labeled
276 tRNA did not inhibit peptide dissociation.

277 Ensemble fluorescence anisotropy results using Atto(pep)-Stop-POST5

278 The fluorescence anisotropy of the pentapeptidyl moiety of Atto(pep)-Stop-POST5 is quite high (0.22), and decreases
279 following addition of RFC, providing a convenient measure of the rate of pentapeptide release from the ribosome. Sample
280 results show the time dependence of anisotropy decrease as a function of RFC concentration (Fig. 4e), and, at fixed RFC, of
281 ataluren concentration (Fig. 4f). Each such time-dependent anisotropy decrease could be fit to a single exponential, giving
282 the collected rate constants presented in Fig. 4g, in which the rate dependence as a function of RFC concentration is measured
283 at 0, 200, 500, and 1,000 μM ataluren. In the absence of ataluren, we obtained EC_{50} ($0.029 \pm 0.002 \text{ }\mu\text{M}$) and V_{max} (0.31 ± 0.02
284 s^{-1}) values for pentapeptide release similar to those we measured by smTIRF. In addition, as with the smTIRF results, V_{max}
285 values were unaffected by added ataluren but EC_{50} values increase, reaching $\sim 0.06 \text{ }\mu\text{M}$ at 1000 μM ataluren.

286 Ataluren inhibition of RFC activity is cooperative

287 The observed dissociation rate constants for pentapeptide release, measured by both smTIRF and fluorescence anisotropy,
288 show very similar sigmoidal dependences on added ataluren concentration (Fig. 4h), giving a Hill n value of 3.0 ± 0.6 and a
289 K_A of $250 \pm 20 \text{ }\mu\text{M}$ (see eq 3). Similar results were obtained for tRNA release measured by smTIRF (Hill $n = 2.7 \pm 0.4$, K_A
290 $= 180 \pm 10 \text{ }\mu\text{M}$).

291 Further control experiments

292 The rates of complete release of the two products, $\sim 0.2 - 0.3 \text{ min}^{-1}$, observed here at $24 \text{ }^\circ\text{C} - 25 \text{ }^\circ\text{C}$ (Figs. 4 c,d,g,h) are \sim
293 20 -30 times slower than the rate constants of $5 - 10 \text{ min}^{-1}$ at $30 \text{ }^\circ\text{C}$ for cleavage of the peptidyl-tRNA ester linkage by the
294 RFC on yeast ribosomes (36, 37), raising the question of whether the slow rates we find might be an artifact due to interactions
295 that the dyes attached to the peptide and the tRNA might make with the ribosome. With respect to the effect of Atto 647
296 labeling of the peptide, we tested this point directly by determining the rate of dissociation at $25 \text{ }^\circ\text{C}$ of a radioactively labeled
297 peptide devoid of any fluorescent label. Here we employed a Millipore filtration assay in which the cleaved peptide,
298 noncovalently bound to the ribosome, is retained on the filter, while the released peptide is found in the filtrate. As
299 demonstrated in Fig. 4i, the rate constants measured by determining the radioactivity either retained on the filter (0.30 ± 0.07)
300 or found in the filtrate (0.19 ± 0.05) match well the peptide release rates determined in our fluorescent assays (Fig. 4c,g).
301 Given the close similarity in the measured rates of fluorescent Cy3-labeled tRNA^{Gln} dissociation and peptide dissociation,
302 which is mechanistically significant (see Discussion), we think it extremely unlikely that the Cy3 labeling significantly retards
303 tRNA^{Gln} dissociation. This view is buttressed by the much smaller relative structural change that dye labeling of tRNA
304 represents as compared with dye labeling of a pentapeptide. In other control experiments, we found that addition of ataluren
305 before RFC or simultaneously with RFC gave equivalent results, in both sm-TIRF and ensemble fluorescence anisotropy

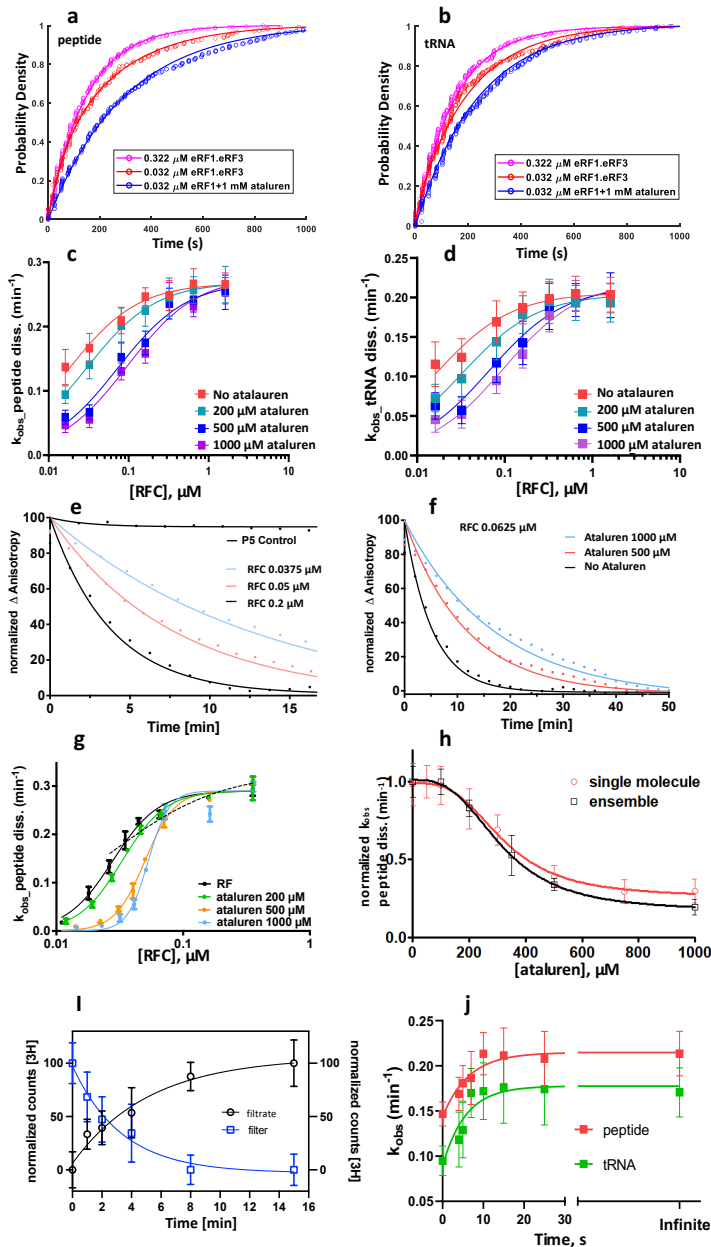


Figure 4. **a.** and **b.** Cumulative distributions of **a.** peptide and **b.** tRNA dissociation times at indicated RFC concentrations, one also with 1 mM ataluren. Each cumulative distribution is constructed from ≥ 300 kinetic traces. **c.** and **d.** Rates of dissociation of **c.** peptide and **d.** tRNA as a function of RFC concentration at different fixed ataluren concentrations. Error bars are \pm s.e.m. from 250- 750 trials. **e.** and **f.** Normalized plots of ensemble experiments showing single exponential fits (solid lines) of decimated smoothed raw data (points) of atto647 pentapeptide release reaction measured by fluorescence anisotropy decay vs. time at 25 $^{\circ}\text{C}$. **e.** At indicated RFC concentrations. The control shows the near constancy of observed anisotropy in the absence of added RFC or ataluren. **f.** At an RFC concentration of 0.0625 μM and varying ataluren concentrations. **g.** The rates of dissociation of atto647 pentapeptide in ensemble experiments as a function of free RFC concentration at varying ataluren concentrations. Error bars are average deviation (a. d.) for 2 – 6 independent determinations. **h.** Ataluren inhibition of normalized rates of dissociation of atto647 pentapeptide as measured by single molecule (red) and plate reader (black) assays. [eRF1], 32 nM; [eRF3], 0.2 μM and 0.8 μM in the single molecule and ensemble assays, respectively. Error bars are \pm s.e.m. ≥ 250 trials (single molecule) and \pm a.d., 2 independent determinations (plate reader). **i.** Rates of dissociation of atto647 labeled and unlabeled pentapeptide as measured by millipore filtration, calculated using both filtrate and filter retained values. Error bars are \pm a.d. for 8 independent measurements. [eRF1], 0.2 μM ; [eRF3], 0.8 μM ; POST5, 0.05 μM . **j.** Ataluren inhibition of peptide and tRNA release when added at different times (4 - 25s) following RFC addition to Stop-POST5. [RFC], 0.08 μM ; [Ataluren], 1 mM. Values at zero-time correspond to simultaneous addition of ataluren and RFC. Error bars are \pm s.e.m. ≥ 200 trials.

307 experiments consistent with the notion that ataluren binds more rapidly to Stop-POST5 complex than does the RFC. In
 308 addition, very similar results were obtained in the fluorescence anisotropy experiments with POST5 complexes prepared by
 309 combination of isolated 40S and 60S subunits or from 80S ribosomes salt-treated to facilitate IRES binding, as described in
 310 Materials and Methods.

311 **Ataluren has no direct effects on the rates of peptide and tRNA release, processes which proceed much more slowly**
 312 **than tRNA-peptide bond cleavage.**

313 Cleavage of the tRNA-peptide ester linkage by the RFC has been reported to proceed on yeast ribosomes with rate constants
 314 of 5 -10 min⁻¹ at 30 °C, determined using a thin layer electrophoresis assay (36, 37), much faster than the rates of complete
 315 release of the two products, ~0.2 - 0.3 min⁻¹, observed here (Figs. 4c,d,g,h). We reasoned that if ataluren inhibits the tRNA-
 316 peptide bond cleavage solely by competition with RFC, then the time course of tRNA-peptide hydrolysis might be tracked
 317 by adding ataluren at fixed times after RFC addition. Using two syringe pumps triggered at pre-programmed times after
 318 camera recording started, Stop-POST5 was treated first with 0.081 μM RFC. Subsequently, 1000 μM ataluren was added to
 319 the flow chamber at times varying from 4 - 25 s. k_{RF} values for peptide and tRNA dissociation are plotted vs. the interval
 320 between RFC and ataluren addition in Fig. 4j. Zero time in this plot indicates simultaneous addition of RFC and ataluren.
 321 Infinite time indicates no addition of ataluren. The rate constants for elimination of ataluren's inhibitory effect after RFC
 322 addition are 10.8 ± 3.6 min⁻¹ and 9.6 ± 2.6 min⁻¹ for tRNA and peptide respectively, measured at 24 °C. These values are
 323 fully compatible with the rate constants reported for peptidyl-cleavage on yeast ribosomes mentioned above (36, 37).

324 **Correlation between individual peptide and tRNA release times**

325 We next tested whether tRNA and peptide release were linked or independent of one another by calculating the correlation
 326 coefficient between peptide and tRNA release times for each ribosome measured in the single molecule experiments. By
 327 correlating these times, it was possible to determine whether release of peptide accelerated or retarded tRNA release and,
 328 conversely, whether release of tRNA altered the rate of peptide release. Fluorescence excitation laser powers were reduced
 329 to 10-20% of that in the other experiments to minimize distortion of any correlation between the release times caused by
 330 photobleaching, which is not expected to be correlated between

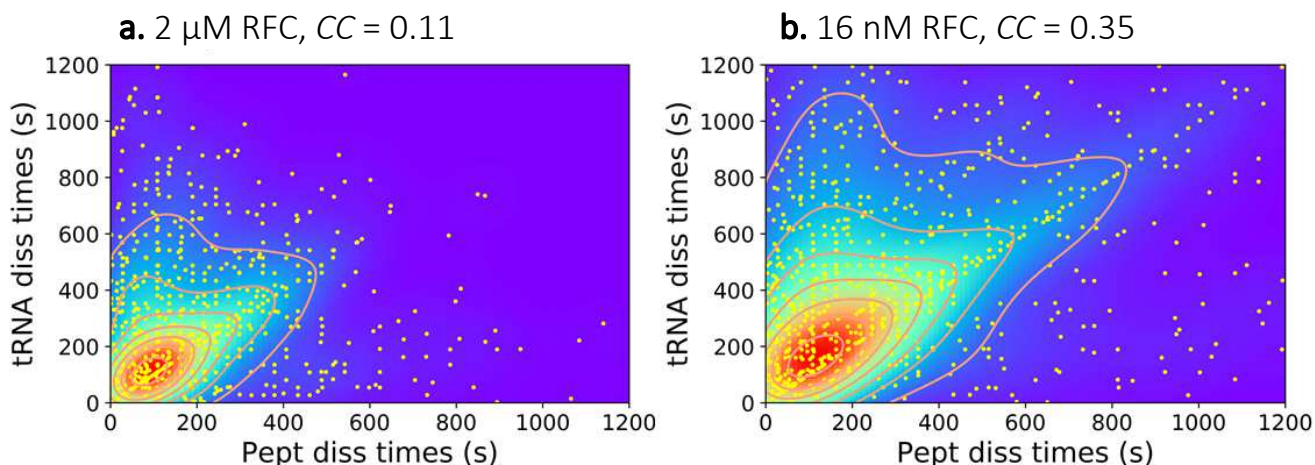


Figure 5. Scatter plots of peptide and tRNA dissociation times. Each point represents dissociation times from an individual ribosome. CC is correlation coefficient. **a.** 2 μM RFC. **b.** 16 nM RFC.

331 the Cy3-tRNA and Atto647-peptide labels. Fig. 5 shows scatter plots of individual tRNA lifetimes vs. the corresponding
 332 peptide lifetimes for each particle, as well as contour plots of these distributions. Correlation coefficients (CC) between the
 333 peptide and tRNA lifetimes were calculated using eq. (3)
 334

335

$$CC = \frac{n \sum t_i p_i - \sum t_i \sum p_i}{\sqrt{n \sum t_i^2 - (\sum t_i)^2} \sqrt{n \sum p_i^2 - (\sum p_i)^2}} \quad (3)$$

336 where t_i and p_i are individual tRNA and peptide lifetimes after RFC addition, respectively, and the summations are conducted
337 over n individual events. CC would equal 1.0 if the two products always dissociated together, fall between 0 and 1 if a
338 preceding slow step limits both events or if dissociation of one product accelerates dissociation of the other, and be < 0 if
339 dissociation of one slows dissociation of the other. We found CC to be approximately 0.11 ± 0.03 at saturating RFC and 0.3
340 $- 0.4$ at 16 nM RFC. This value suggests that dissociation times of the two ligands are partly limited by a preceding common
341 kinetic step in the pathway and partly by the two independent (microscopic) dissociation rates. The higher CC at low RFC
342 concentration shows the more prominent effect of the slowed preceding reactions, leading to increased correlation of the
343 peptide and tRNA dissociations. The implications of these results for the kinetic pathway of termination are taken up in
344 Discussion.

345 DISCUSSION

346 Recently we demonstrated that ataluren stimulation of nonsense codon readthrough results exclusively from its inhibition
347 of RFC-dependent termination of polypeptide synthesis and does so via apparent binding to multiple, probably at least three,
348 sites of the protein synthesis apparatus (27). Here, using both single molecule and ensemble measurements of release factor
349 activity, we demonstrate that cooperative binding of ataluren to these sites, proceeding with a Hill n of 3.0 ± 0.6 and an EC_{50}
350 of 340 μM , competitively inhibits RFC catalysis of termination (Fig. 4h). We also employ AzAt, a structural (Fig. 1a) and
351 functional (Supplementary Fig. 1) (21) photolabile analogue of ataluren, to identify two of these ataluren sites within rRNA
352 by photoincorporation of AzAt. One of these sites, 18S-A1195, is proximal to the ribosome decoding center (Fig. 2g). Both
353 eRF1.eRF3.GDPNP and ataluren inhibit AzAt photoincorporation into this site (Table 1), providing strong evidence that it is
354 a site linked to ataluren inhibition of termination. The second site lies within the PTC (Fig. 2h), where the termination
355 hydrolysis reaction takes place, and is identified by AzAt photoincorporation into nucleotides 26S-A2669, 26S-A2672, and
356 26S-A3093. This photoincorporation proceeds cooperatively, with a Hill n of 3.3 ± 0.2 and an EC_{50} of 200 μM (Fig. 2e).
357 Compelling evidence that ataluren binding to the PTC is important for inhibition of termination is provided by the similarities
358 in the Hill n and EC_{50} values for both ataluren inhibition of termination and AzAt photoincorporation into the PTC, as well
359 as by the inhibition of AzAt photoincorporation by eRF1.eRF3.GDPNP (Table 1).

360 Two important unknowns remain concerning ataluren inhibition of termination. One is the identity of a likely third
361 ataluren site important for inhibition. The binding site within eRF1 identified by AzAt photoincorporation (Fig. 2b,c) is a
362 possible candidate. Although ataluren binding to this site does not affect V_{max} values for peptide and tRNA departure from
363 the ribosome (Figs. 4c,d,g), it could inhibit termination by weakening RFC binding to the ribosome. However, we currently
364 lack evidence that this is the case. Other possibilities would include a site within a ribosomal protein, which remains to be
365 determined, or an additional site within the RNA fraction of Stop-POST5. For example, a site which had a low yield of AzAt
366 photoincorporation would not have been included within the 22 nucleotides shown in Fig. 2d. In addition, a site within the
367 22 nucleotides which was excluded from further consideration because of the proximity to eRF1 criterion that we imposed,
368 but which allosterically inhibited eRF1 binding. The second unknown is the mechanism underlying the cooperative nature of
369 ataluren binding seen in Figs. 2e and 4h. It is reasonable to posit that ataluren binding to a site or sites other than the PTC
370 induces a conformational change within the Stop-POST5 complex which stimulates ataluren binding to the PTC. 18S-A1195
371 is a plausible candidate for such a site, since AzAt photoincorporation into 18S-A1195 proceeds noncooperatively, and with
372 a lower EC_{50} than that seen for photoincorporation into the PTC. Structural studies directed toward determining whether
373 ataluren induces such a structural change, and, if so, through binding to which sites, could elucidate this mechanism.

374 In cryoelectron microscopy structures of the eRF1.eRF3.GDPNP (38) or eRF1.eRF3.GDPCP (35) bound to
375 pretermination complexes similar to POST-Stop5, eRF1 is bound to eRF3 in a conformation preventing it from extending
376 into the PTC, while interacting strongly with the 18S rRNA decoding center. These structures raise the question of why we
377 detect inhibition by added eRF1.eRF3.GDPNP of AzAt photoincorporation at both sites. This seeming inconsistency is
378 resolved by recent single molecule experiments (37) showing that the binding to a pretermination complex of a modified
379 RFC complex, formed either with a GTPase-deficient eRF3 variant or with GTP- γS in place of GTP, is followed by rapid
380 dissociation ($< 3\text{s}$) of eRF3 from the ribosome, even in the absence of GTP hydrolysis. In our photoincorporation experiments,
381 rapid dissociation of eRF3.GDPNP would allow the eRF1 bound to the ribosome to adopt the elongated conformation that

382 interacts with both the PTC and the decoding center (32, 33) during the minute-long photoincorporation process
 383 (Supplementary Fig. 12). It remains unclear why eRF3 is still bound to the ribosome in the cryo-EM structures.

384 Although uncertainties remain in our understanding of the termination process, we think it useful to present a highly
 385 simplified and only semi-quantitative kinetic scheme (Fig. 6) for termination of peptide synthesis and its inhibition by
 386 ataluren, consistent with the results presented above. The results in Fig. 4 show that ataluren is an apparent competitive
 387 inhibitor of RFC catalysis of tRNA and peptide release but only acts on steps up to or including the cleavage reaction. This
 388 accounts for the placement of ataluren binding prior to formation of complex C1. For simplicity we show n molecules of
 389 ataluren binding in a single step, and, in the cartoon, indicate two of the binding sites identified by our photoaffinity labeling
 390 results as being in the 40S decoding center and the 60S PTC. In this scheme the relatively rapid cleavage step leading to
 391 complex C2 proceeds with a rate constant of 10 min^{-1} . The much slower tRNA and peptide release steps from complex C3
 392 proceed with similar apparent constants of 0.2 to 0.3 min^{-1} at saturating RFC concentration. Recent results of others under
 393 conditions comparable to ours indicate that eRF1 dissociates with a rate constant, $0.2 - 0.3 \text{ min}^{-1}$ from a yeast ribosome
 394 following the cleavage reaction (37), quite similar to the rate constants we measure for peptide and tRNA release. This
 395 similarity suggests that all three dissociations proceed via a hypothetical common intermediate (C3, in brackets), possibly
 396 involving a conformational change, which is at least partially rate-determining for each dissociation. The presence of C3 in
 397 the kinetic scheme is consistent with the positive CC value of ~ 0.1 we have determined, which results in a value of k_c
 398 approximately equal to 3 times the value of either k_{t1} or k_{p1} (see Supplementary Notes). We conclude that peptide and tRNA
 399 each have their own activation energy barrier for release. Further work will be required to determine how closely, if at all,
 400 eRF1 release is coordinated with either peptide or tRNA release.

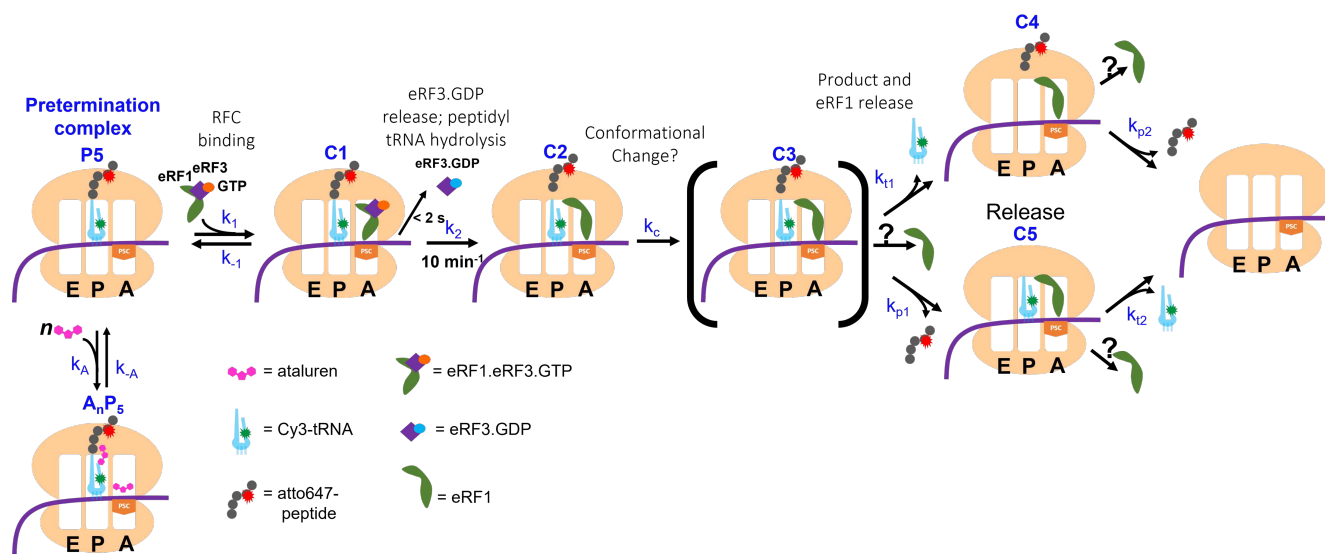


Figure 6. A simplified model for RFC catalysis of termination. This model, consistent with all of our results, as well as with recent published results of others (30), posits that ataluren inhibition results from the cooperative binding of n molecules of ataluren to the pretermination complex P5 in competition with RFC binding. It also invokes a hypothetical complex C3 resulting from an at least partial rate-determining conformational change, following cleavage of the tRNA-peptide ester bond to account for the similarity in the rate constants of tRNA, peptide, and eRF1 release (see text). The question marks associated with possible eRF1 release are shown to indicate our current uncertainty as to whether eRF1 release is coordinated with either peptide or tRNA release, or proceeds independently of either.

401

402 The pentapeptide release we observe could occur directly from the PTC or via the peptide tunnel, as is the case for much
 403 longer peptides. In support of release via the peptide tunnel is the close similarity between our measured rate constant of
 404 peptide release (0.3 min^{-1} , Fig. 4) and that measured at $30 \text{ }^\circ\text{C}$ for release of a full-length nanoluciferase protein, synthesized
 405 in a rabbit reticulocyte lysate, following RFC-dependent termination (0.35 min^{-1}) (39). This similarity also provides a strong
 406 indication that our results showing that product release is rate-determining for termination is likely to be physiologically
 407 relevant, since typical cellular concentrations of both eRF1 and eRF3 (40) are considerably in excess of our measured EC_{50}

408 values for RFC of 20 - 30 nM. Nevertheless, given the direct coupling of eukaryotic termination with ribosome recycling
409 (41), it will be of interest to determine the effect of adding recycling factors (e.g., Rli1p, ABCE1) on the rates of product
410 release, and experiments to elucidate this point are underway.

411 The EC₅₀ values for ataluren measured in this paper and in our earlier work (21, 27) cluster in the range of 150 – 300 μM,
412 ~10 to 30 times higher than ataluren concentrations employed in the growth media typically used in studies of ataluren
413 stimulation of read-through in intact cells or tissue cultures (42, 43). As we pointed out earlier (27), this difference may be
414 more apparent than real, since ataluren, like other hydrophobic molecules, could be preferentially taken up by cells, such that
415 its cellular concentration far exceeds that present in the cell culture medium (44). Nevertheless, it would clearly be desirable
416 to develop future TRIDs with greater potency than ataluren for combatting PSC diseases. Elsewhere (27) we have argued
417 that such development should favor TRIDs directed toward inhibiting termination. In that work we showed that even a high
418 concentration (500 μM) of ataluren does not interfere with the binding of near-cognate Trp-tRNA^{Trp}.eEF1A.GTP ternary
419 complex (TC) to Stop-POST5 during the readthrough elongation cycle. Our present results demonstrate that, in contrast,
420 ataluren binding to both the decoding center and the PTC (Figs. 2g,h) competitively inhibits RFC binding to Stop-POST5
421 (Figs. 4c,d,g), even though TC and RFC binding sites to pretermination complexes like Stop-POST5 have considerable
422 overlap (35). While our results are insufficient to precisely locate the ataluren sites within the ribosome, our working
423 hypothesis is that they will lie in areas of the RFC binding site proximal to the decoding center and the PTC which *do not*
424 overlap with the TC binding site. This leads us to suggest that, in the current absence of high resolution structures of ataluren
425 sites, efforts to design TRIDs with higher affinity for pretermination complexes than ataluren should focus on these non-
426 overlapping sites.
427

428 MATERIALS

429 [³H]-AzAt was prepared by catalytic tritiation (Vitrex, Placentia, CA) of 3-[5-(4-azidophenyl)-1,2,4-oxadiazol-3-yl]-6-iodo
430 benzoic acid (6-iodo-AzAt). The chemical purity of the tritiated product was verified by its comigration with authentic AzAt
431 on RP-HPLC analysis (Supplementary Fig. 13). AzAt and 6-iodo-AzAt were supplied by PTC Therapeutics. Both compounds
432 were characterized by ¹H NMR [(DMSO-d₆, 500 MHz): *AzAt*, δ 13.35 (br, s, 1H), 8.6-8.7 (m, 1H), 8.32 (d, 1H, *J*=7.6 Hz),
433 8.2-8.3 (m, 2H), 8.1-8.2 (m, 1H), 7.75 (t, 1H, *J*=7.6 Hz), 7.3-7.5 (m, 2H); *6-iodo-AzAt*, δ ppm 13.67 (br s, 1 H) 8.36 (s, 1 H)
434 8.16 - 8.29 (m, 3 H) 7.89 (br d, *J*=7.32 Hz, 1 H) 7.38 (br d, *J*=8.24 Hz, 2 H) and mass spectroscopy [*AzAt*, 306.4 [M-H]⁻,
435 exact mass 307.07; *6-iodo-AzAt*, 432.2 [M-H]⁻, exact mass 432.97] and each ran as a single peak on RP-HPLC analysis
436 (Supplementary Fig. 13). Atto647-N-hydroxysuccinimide ester (Atto647-NHS) was obtained from Sigma-Aldrich.

437 **Atto 647-ε-lysine tRNA^{Lys} formation.** Atto647-ε-lysine tRNA^{Lys} was prepared by reacting Atto647-NHS with [³H]Lys-
438 tRNA^{Lys} (*S. cerevisiae*) following a procedure based on that used for the preparation of NBD-ε-[³H]Lys-tRNA^{Lys} (45).
439 Briefly, Atto647 NHS ester dissolved in DMSO (38.5 mM, 10 μl) was added quickly to a 50 mM K⁺ phosphate buffer, pH
440 11 (20 μl) and DMSO (50 μl) solution at 25 °C, followed directly by [³H]Lys-tRNA^{Lys} (20 nmol, 165 μM, 120 μl) dissolved
441 in water, reaching a final concentration of 0.1 mM tRNA and 2.0 mM dye at a final pH of 10.8. A color change from dark
442 blue to dark teal was observed. The mixture was stirred in a thermomixer for 4 min at 25 °C, quenched with 4 M acetic acid
443 (17 μl), which restores the original blue color, and directly ethanol precipitated (20% potassium acetate pH 5 (2.7 ml), cold
444 EtOH (17 ml) at -80°C for 1h). Ethanol precipitation was repeated twice to remove any residual Atto647-NHS, and the
445 resulting aqueous solution was stored as an aqueous solution containing diethyl pyrocarbonate (0.1%) in small aliquots at -
446 80 °C. The stoichiometry of [³H]-Lys charging was typically 0.35 ± 0.05/tRNA^{Lys}. The stoichiometry of Atto647 labeling,
447 measured by UV absorption (ε₆₄₇: 120000 mol⁻¹ cm⁻¹), was 0.40 ± 0.05/tRNA^{Lys}.

448 **Ribosome complexes.** 80S-S.IRES and Stop-POST5 complexes used in photoaffinity labeling and fluorescence anisotropy
449 experiments were either prepared from shrimp (*Artemia salina*) cyst 40S and 60S subunits, Stop-IRES, aminoacyl-tRNAs
450 (Phe-tRNA^{Phe}, Lys-tRNA^{Lys}, Val-tRNA^{Val}, Arg-tRNA^{Arg}, Gln-tRNA^{Gln}), yeast elongation factors (eEF1A and eEF2), and
451 GTP (photoaffinity labeling and fluorescence anisotropy experiments), as previously described (46), or via a high KCl
452 treatment of 80S ribosomes (fluorescence anisotropy experiments). In the latter case, crude 80S ribosomes were dissolved

453 in Buffer 4 (40 mM Tris HCl, pH 7.5, 80 mM NH₄Cl, 5 mM Mg(Ac)₂, 100 mM KOAc, and 3 mM β-mercaptoethanol). and
454 pelleted by microultracentrifugation for 1h at 540,000 x g at 4 °C. The washed 80S ribosomes (2 μM) were combined with
455 Stop-IRES (4 μM) in Buffer 4 supplemented with added 0.4 M KCl and incubated at 37 °C for 30 min. The resulting
456 80S.Stop-IRES complex was ultracentrifuged through a 1.1 M sucrose solution in Buffer 4 (1.65x of reaction volume) for
457 1h at 540,000 x g at 4 °C, and the pellet was dissolved in Buffer 4 and stored in small aliquots at -80 °C. This preparation
458 of 80S.Stop-IRES complex was used to make Stop-POST5 complex by a process essentially identical to that used for
459 converting 80S.Stop-IRES made from 40S and 60S subunits to Stop-POST5 complex (46).

460 80S.IRES concentrations were estimated by A₂₆₀ measurement, while the concentration of Stop-POST5 was estimated
461 from both the A₂₆₀ measurement and the stoichiometry of radioactively labeled pentapeptide per 80S ribosome. Typically, 40
462 ± 5 % of the 80S ribosome harbors the pentapeptide. For Atto(pep)-Stop-POST5 and Atto(pep)-Cy-Stop-POST5 preparation,
463 Atto647-□ measurement^{Lys} replaced lysine-tRNA^{Lys}. Also, for Atto(pep)-Cy-Stop-POST5 and Atto(rbsm)-Cy-Stop-POST5
464 preparation, Gln-tRNA^{Gln}(Cy3) replaced Gln-tRNA^{Gln}. Finally, for Atto(rbsm)-Cy(tRNA)-Stop-POST5 and Atto(pep)-
465 Cy(ribsm)-Stop-POST5 preparation, ribosomes labeled on r-protein Lys residues to an average stoichiometry of 0.82
466 Atto647/ribosome and 0.95 Cy3/ribosome, respectively, replaced unlabeled ribosomes. Such labeled ribosomes were
467 prepared using a previously published method for *E. coli* 70S ribosome labeling with minor modification (47). In brief,
468 labeling was performed in LB buffer (40 mM HEPES, pH 7.5, 80 mM NH₄Cl, 5 mM Mg (Ac)₂, 100 mM KOAc). A sample
469 of crude 80S shrimp ribosomes, was layered on top of 1.1M sucrose in LB, then spun at 540,000 x g for 90 min. The pellet
470 was washed three times with LB and then dissolved again in LB. For the labeling reaction, a 2-fold molar excess of Atto647N-
471 NHS ester (ATTO-TEC GMBH, dissolved in DMSO) and a 4- fold molar excess of Cy3-NHS ester (Lumiprobe, dissolved
472 in DMSO) was incubated with 5 μM 80S ribosome in LB at 37 °C for 30 mins with stirring. After the reaction, the reaction
473 mixture was layered on the top of 1.1M sucrose in Buffer 4, then spun at 540,000 x g for 90 min. The labeled ribosome pellet
474 was dissolved in Buffer 4. A final spin at 11,952 x g for 2 min removes residual contaminants. The labeling efficiency was
475 calculated by using the molar extinction coefficients of 80S ribosome at 260 nm of Atto647N-NHS ester at 647 nm and of
476 Cy3-NHS ester at 555 nm.

477 For the single-molecule experiments, Stop-POST5 was prepared from 40S and 60S subunits and Stop-IRES mRNA
478 covalently attached to biotin at its 3' end, as described (48), with the following modifications. The oxidation of mRNA was
479 performed in a solution containing mRNA at a concentration of 10–50 A₂₆₀/ml, 100 mM sodium acetate (pH 5.2), and 90 mM
480 sodium m-periodate (prepared fresh). After a 2-hr incubation at room temperature, the periodate was precipitated by adding
481 KCl to a final concentration of 200 mM and incubating for 5 minutes on ice. The precipitate was removed by centrifugation
482 for 5 minutes at 10,000 g, 2°C and passage of the supernatant through a Sephadex G-25 column (Nap-5, Pharmacia). EZ-
483 Link hydrazide biotin (ThermoFisher, inc.) was then added to a final concentration of 2 mM from a 50 mM stock in DMSO
484 (prepared fresh). The biotinylation reaction was carried out for 2 hours at room temperature, after which the whole mixture
485 was applied to a Sephadex G-25 column (PD-10, Pharmacia), the high molecular weight fractions were precipitated by ethanol
486 addition, and the resulting pellet pellet was dissolved in DEPC treated H₂O. The concentration of biotinylated mRNA was
487 determined by A₂₆₀.

488 *S. cerevisiae* eEF1A and eEF2 preparations were adapted from the eEF2 preparation method described previously (21,
489 27, 46). Full-length *S. cerevisiae* eRF1 and amino acid residues (166-685) of the eRF3 open reading frame sequences were
490 inserted into the pET-15b (Novagen) plasmid obtained from the laboratory of Allan Jacobson (University of Massachusetts
491 Medical School). eRF1 and eRF3 plasmids were transformed into the *E. coli* BL21(DE3) CodonPlus (Agilent) strain in the
492 presence of ampicillin. eRF1 and eRF3 were isolated from cell lysate as described earlier (21, 27, 46).

493 **TRIDs.** Ataluren sodium salt and GJ072 were obtained as gifts from PTC Therapeutics.

494 **tRNAs.** Yeast tRNA^{Phe} was purchased from Sigma-Aldrich. Other isoacceptor tRNAs were prepared from bulk tRNA
495 (Roche) from either *E. coli* (tRNA^{Val}, tRNA^{Lys}, tRNA^{Gln}, and or *S. cerevisiae* (tRNA^{Arg}, via hybridization to immobilized
496 complementary oligo DNAs as described previously (49, 50). *E. coli* and yeast tRNAs were charged with their cognate amino
497 acids as described (21, 27, 46).

498 **METHODS**

499 **Photoaffinity labeling with [³H]-AzAt.** eRF1, eRF1.eRF3.GDPNP, Stop-POST5, and 80S.IRES samples in Buffer 4,
500 typically 20 μL, were incubated in the dark (20 min for Stop-POST5 and 80S.IRES complexes, 2 min for release factors)
501 with various concentrations of [³H]-AzAt at 37 °C, transferred to a UV-transparent cuvette which was covered with parafilm
502 to prevent evaporation, and irradiated in a Rayonet photochemical reactor equipped with 300 nm UV lamps for 5 min at room
503 temperature. This was followed by quenching with 2 mM DTT at 37 °C for 5 min under ambient light. The irradiation time
504 gave complete photolysis of the phenyl azide moiety in AzAt (Supplementary Fig. 12). Photolysis was also complete at 5
505 min in the presence of 1 mM ataluren (Supplementary Fig. 14), ruling out internal filtering effects.

506 Stop-POST5 and 80S.IRES complexes. 1 μM solutions of either Stop-POST5 or 80S-S.IRES, determined by A₂₆₀, were
507 photolabeled by [³H]-AzAt. The sample was then either directly purified by ultracentrifugation through a sucrose cushion to
508 determine the photoincorporation stoichiometry in the complex, or subjected to phenol/chloroform extraction to determine
509 the photoincorporation stoichiometry in the total RNA. To determine the photoincorporation background arising from
510 incomplete removal of noncovalently bound photolyzed AzAt, AzAt was prephotolysed for 5 min before adding to the
511 complex, followed by the 20 min incubation in dark at 37 °C and subsequent sucrose cushion purification or RNA extraction
512 as described above. This background level, which never exceeded 17 ± 3% of what was observed for the photoincorporation
513 experiment, was subtracted from the observed values in the reported results.

514 Photoaffinity labeling of release factors. Solutions containing eRF1 (10 μM), eRF3 (20 μM) and 1mM GMPPMP were pre-
515 incubated at 37 °C for 2 min to form the ternary complex prior to photolabeling with [³H]-AzAt. After quenching, reaction
516 mixtures were loaded onto a 4-15% mini protean SDS-PAGE gel for protein separation and isolation. Gel slices containing
517 eRF1 or eRF3, as shown by Coomassie Blue R250 staining were crushed and the radioactivity was extracted in extraction
518 buffer (50 mM Tris-HCl, 150 mM NaCl, and 0.1 mM EDTA; pH 7.5) by vigorously shaking at 70 °C for 30 min. The data
519 fitting was performed using the software Prism. Labeling results of eRF1 alone and within the eRF1.eRF3.GDPNP complex
520 were fit with a one-site binding model and a two-site binding model, respectively.

521 **RNA-Seq** procedures employed closely follow those published (29, 51) except as noted.

522 Library preparation. RNA-seq libraries were prepared for PAL, PRE, UV, and NUL samples, as defined in Results, of Stop-
523 POST5 and 80S.IRES complexes, using published procedures (29, 51) with the slight modifications that a 12% 0.13 M
524 Tris/45mM Borate/2.5mM EDTA (pH 7.6)- Urea PAGE gel replaced a 10% PAGE gel and the selected RNA fragment size
525 was 40-70 bp rather than 60-70 bp. In brief, RNA was extracted and randomly fragmented by ZnCl₂ (Sigma). After separation
526 on the TBE-Urea PAGE gel, RNA fragments, visualized by ethidium bromide staining (used for all RNA gels) were sliced
527 and extracted from the gel by crushing the gel and vigorously shaking at 70 °C in 400 μL of water for 15 min. The 3' ends
528 were dephosphorylated by T4 Polynucleotide Kinase (New England Biolab). The miRNA cloning linker 2
529 (5'App/CACTCGGGCACCAAGGA/3'ddC, Integrated DNA Technologies) was used as the universal 3' linker and pre-
530 adenylated using the 5' DNA Adenylation Kit (New England Biolab) with the provided protocol. Reverse transcription, self-
531 circularization, and PCR amplification were performed essentially the same as previously described (51). Library sequencing
532 was performed with Illumina NextSeq with single-end mode for up to 75 bp read length.

533 Data processing. Sequencing reads were processed by Cutadapt 2.10 (<https://cutadapt.readthedocs.io/en/stable/>) to remove 3'
534 end linkers and then read into Shapemapper2 (52) to count the mutations and effective sequencing reads, using the STAR
535 Aligner mode (53) The mutation rate of each nucleotide was calculated by dividing the number of the reads containing the
536 mutations by the total number of reads, outputted as N.

537 For the PAL sample, the mutation rate fold change was calculated by dividing the mutation rate of the PAL sample by
538 the mutation rate of the PRE sample. The average mutation count was calculated by averaging the number of mutations of
539 the PAL and PRE samples. MA plots (Supplementary Fig. 6) were displayed by plotting the mutation rate fold change of
540 each nucleotide as a function of the average mutation count of each nucleotide. To determine possibly significant sites of
541 AzAt labeling, the dataset was first screened for points that meet the criteria of a mutation rate fold change ≥ 1.5 and an
542 average mutation count ≥ 100. Points meeting these criteria were further screened with Z-factor>0 and p-value<0.05 to
543 determine statistical significance. The Z-factor (z) was calculated using eq. 4.

544

$$z = 1 - \frac{1.96 \times (\sigma_{PAL} + \sigma_{PRE})}{|\Delta N|} \quad (4)$$

545

546

547

σ is the square root of the mutation rate (M) divided by the read depth (C) and further normalized by the average mutation rate (A): $\sigma = \sqrt{(M/C)/A}$. ΔN is the difference in the normalized mutation rate ($N = M/A$) between the PAL and PRE samples.

548

549

550

551

552

553

To determine the impact of UV treatment, the mutation rate fold change was calculated by dividing the mutation rate of the UV sample by the mutation rate of the NUL sample. The delta mutation rate (UV-NUL) was also calculated as an extra layer of filtering. Nucleotides having >10 UV/NUL, >0.01 (UV – NUL), and >100 average mutation counts were selected, and identified by sequence homology within the yeast rRNA sequence (Supplementary Table 4). Native rRNA modifications within the Stop-POST5 (NUL) and 80S.IRES (NUL) samples having ≥ 0.2 average mutation rate were similarly identified within the yeast rRNA sequence (Supplementary Table 2).

554

555

556

557

558

559

560

561

562

563

564

RNaseH Fragment Assay. RNA was prepared from the ^3H -AzAt photoaffinity labeled ribosome by phenol-chloroform extraction. RNA: DNA duplexes were formed by incubating total RNA (0.2 μM) with an oligonucleotide pair (1 μM of each, sequences shown Supplementary Table 4), flanking a specific RNA region, in 22.8 μL of water at 95 $^\circ\text{C}$ for 2 min, followed by annealing at 50 $^\circ\text{C}$ for 30 s and quenching on ice. Six units (1.2 μL) of RNase H (NEB) and 6 μl of 5x RNase H Reaction Buffer were next added to the RNA: DNA duplex and incubated at 37 $^\circ\text{C}$ for 1 hour, followed by phenol-chloroform extraction of RNA. The digested RNA was separated on a 12% TBE-Urea PAGE gel, and the target band along with the adjacent upper and bottom gels were sliced by a 2 mm gel cutter. The gel slices were crushed and the ^3H labeled rRNA fragment was extracted in water by vigorously shaking at 70 $^\circ\text{C}$ for 30 min, or by overnight extraction in elution buffer (0.3 M sodium acetate, 0.25% SDS, 1mM EDTA). The slurry was removed by centrifugation and the eluted [^3H]-labeled rRNA in the supernatant was quantified. The stoichiometry of AzAt photoincorporation was calculated based on a gel recovery yield of $20 \pm 2\%$, determined using an authentic sample of [^3H]-Gln-tRNA^{Gln}.

565

Plate reader anisotropy assay

566

567

568

569

570

571

572

573

574

575

Plate reader assays were run in a Tecan F200[®] 96-well plate reader (Greiner[®] black, non-binding, chimney flat) equipped with 640 nm excitation and 700 nm polarization filters using 96-well plates. Atto(pep)-Stop-POST5 in Buffer 4 (0.1 μM , 80 μl) containing GTP (1 mM) was added to plate wells \pm ataluren at 25 $^\circ\text{C}$. eRF1 and eRF3 aliquots stored at -80 $^\circ\text{C}$ were thawed for 15 s at 37 $^\circ\text{C}$ and added directly to a premade ice-cold GTP (1 mM) \pm ataluren solution in Buffer 4. The resulting release factor solution was incubated at 25 $^\circ\text{C}$ for 1 min, and then added quickly in 80 μL portions to the Atto(pep)-Stop-POST5 containing wells with a multichannel pipette to the Atto(pep)-Stop-Post5 wells. The final concentrations were: eRF1, 0.025 – 0.4 μM ; eRF3, 0.8 μM ; Atto(pep)-Stop-Post5, 0.05 μM . Fluorescence anisotropy decay graphs were fit with GraphPad Prism, using the one phase decay model to obtain peptide dissociation rates. All measurements shown in Figs. 4g,h were independently repeated between 2 and 6 times (average 3.3 times) with error ranges determined as average deviations. The number of independent observations for each curve in Figs. 4g,h varied between 16 – 34.

576

Millipore filtration assay

577

578

579

580

581

582

583

584

585

586

Stop-POST5 complex containing [^3H]-labeled peptide (0.1 μM , 10 μl) in Buffer 4 containing 1 mM GTP was prepared separately for each time point. Release factor mixture in Buffer 4 (eRF1, 0.4 μM ; eRF3, 1.6 μM ; GTP 1 mM) was prepared and kept on ice. A nitrocellulose filter (MF-Millipore, 0.45 μM , MCE Membrane, 25 mm diameter, hydrophilic) was wetted with Buffer 4 for at least 15 seconds and placed on a fritted vacuum filter funnel with a scintillation vial in the vacuum flask for filtrate collection. Stop-POST5 and RF vials were warmed for 1 min at 25 $^\circ\text{C}$ and mixed (for 0 time point Buffer 4 was used), giving the following final concentrations: Stop-POST5, 0.05 μM ; eRF1, 0.2 μM ; eRF3, 0.8 μM . At indicated times, aliquots were applied to the filter, and the filter was immediately washed with Buffer 4 (200 μl). The filtrate and wash were collected in a scintillation vial. The filter was placed in a separate vial and shaken with ethyl acetate (1 ml) for 1h. The fritted vacuum filter funnel was washed three times with Buffer 4 (200 μl) into the filtrate/wash scintillation vial. Scintillation fluid was added to the vials (4 ml), shaken vigorously and radioactivity was determined.

587

Single molecule experiments

588 **Preparation of PEG-passivated slides.** PEG-passivated slides were prepared according to previously published procedures
589 with minor modifications (54). In brief, slides and coverslips were sonicated at 40°C in the order of acetone (10 min),
590 methanol (10 mins), 200 mM KOH (20 min), and ethanol (10 min). Cleaned slides and coverslips were treated in a fume
591 hood with 1 ml 3-aminopropyltriethoxysilane, 5 ml acetic acid, in 94 ml methanol at room temperature overnight, sealed with
592 parafilm, and then incubated with polyethylene glycol (PEG, Laysan Bio, Inc., containing 20% (w/w) mPEG succinimidyl
593 valerate, MW 2000 and 1% biotin-PEG-SC, MW 2000) in 0.1 M sodium bicarbonate (pH 8.3) for 4 h. Slides and coverslips
594 were then washed with Milli-Q water, dried by clean N₂, placed in 50 ml Falcon tubes, vacuum-sealed under N₂ in food saver
595 bags, and stored at -20 °C.

596 **Flow chamber construction.** The flow chambers for fast injection of reaction mixtures were made as described previously
597 (55). The sample flow chambers (8 µL) were formed on slides with holes drilled using a 1.25 mm diamond-tipped drill bit.
598 Polyethylene tubing with 0.97 mm outer diameter (Warner Instruments) was inserted into each hole, sealed with 5 min epoxy
599 and trimmed flush. Double-sided tape laid between the tubes served as spacers and separated the flow chambers. The
600 coverslips were then sealed in place via the double-sided tape and epoxy at their edges.

601 **Immobilization of ribosome Stop-POST 5 complexes.** PEGylated flow chambers were incubated in 0.5 mg/ml streptavidin
602 (Sigma-Aldrich) for 5 mins and washed with Buffer 4. Biotinylated Stop-POST5 containing FK(Atto647)VRQ-tRNA^{Gln}
603 (Cy3) in the P-site, was formed at room temperature by incubating Stop-POST4, containing FK(Atto647)VR-tRNA^{Arg} in the
604 P-site and an empty A-site, eEF1A, GTP, and Gln-(Cy3)tRNA^{Gln} for 5 mins and then injected into the streptavidin-coated
605 slide chamber. After a 5 min incubation, excess unbound ribosome was flowed out. Then eRF1/eRF3 ± TRIDs was injected
606 dynamically at 3 sec while recording. The injection dead time was subtracted for each particle.

607 **Single-molecule fluorescence imaging.** All sm-TIRF studies were carried out at 24 °C. All dilutions, complex formation,
608 and single-molecule imaging were carried out in Buffer 4 with an added enzymatic oxygen scavenging system of 2 mM
609 protocatechuic acid (PCA), 50 nM protocatechunate 3,4 dioxygenase (PCD, Sigma Aldrich), 1 mM cyclooctatetraene (COT,
610 Sigma Aldrich), 1 mM 4-nitrobenzyl alcohol (NBA, Sigma Aldrich), and 1.5 mM 6-hydroxy-2,5,7,8-tetramethyl-chromane-
611 2-carboxylic acid (Trolox, Sigma-Aldrich) (56).

612 Image stacks were recorded at 100 ms frame rate on a custom-built objective-type total internal reflection fluorescence
613 (TIRF) microscope based on a commercial inverted microscope (Eclipse Ti-E, Nikon) and capable of performing alternating-
614 laser excitation (ALEX) between 532 nm and 640 nm laser beams using an acousto-optic tunable filter (AOTF, 50) to switch
615 wavelengths. For the time-lapse experiment, timing of the movies, programmed into NIS-Elements (Nikon) microscope
616 software, were recorded by illuminating the sample for 50 – 20 frames at 10 frames per s with 15 s or 24 s intervening dark
617 intervals. Video recording was started and then eRF1/eRF3 ± TRIDs was injected from a triggered syringe pump at 3 sec
618 during the recording. The injection dead time was subtracted for each particle. Triggering of the shutters, AOTF, and pump
619 was synchronized using LabView scripts driven from the camera exposure signal.

620 **Data analysis.** Collected movies were analyzed by a custom-made software program developed as an ImageJ plugin
621 (<http://rsb.info.nih.gov/ij>). (57), and further analyzed using Python. Distributions of peptide and tRNA dissociation times
622 were fit to eq. 5, using maximum likelihood estimation (58, 59), where P is the probability density.

623
$$P = k_1 e^{-k_1 t} \quad (5)$$

624 Data and fitted curves were plotted as cumulative probability densities. In Figs. 4c,d,h,j the number of kinetic traces in each
625 distribution ranged from 200-750, and the number of independent duplicates ranged from 2-3. Error bars are the mean ± s.e.m
626 which is calculated from the total number of traces.

627 **DATA AVAILABILITY.** The raw sequencing reads fastq data files used in this study are available in the BioProject
628 database under accession code ID PRJNA714648. <https://www.ncbi.nlm.nih.gov/bioproject/?term=PRJNA714648>. An
629 Excel File is available as Supplementary Data 1. The source code programs for single molecule analysis are stored in a
630 Google drive with the following link:

631 https://drive.google.com/drive/folders/1SJnqYL5mWw5O0RrGG_K6L49ztOu03Zjh?usp=sharing

632 All other Source data are provided as Source Data files.

633

634

635 **REFERENCES**

- 636 1. Krawczak, M., Ball, E.V., Fenton, I., Stenson, P.D., Abeyasinghe, S., Thomas, N. and Cooper, D.N. (2000) Human gene
637 mutation database—a biomedical information and research resource. *Hum Mutat*, **15**, 45-51.
- 638 2. Campofelice, A., Lentini, L., Di Leonardo, A., Melfi, R., Tutone, M., Pace, A. and Pibiri, I. (2019) Strategies against
639 Nonsense: Oxadiazoles as Translational Readthrough-Inducing Drugs (TRIDs). *Int J Mol Sci*, **20**.
- 640 3. Mort, M., Ivanov, D., Cooper, D.N. and Chuzhanova, N.A. (2008) A meta-analysis of nonsense mutations causing human
641 genetic disease. *Hum Mutat*, **29**, 1037-1047.
- 642 4. K. Nagel-Wolfrum, F. Möller, I. Penner, T. Baasov, U. Wolfrum, Targeting Nonsense Mutations in Diseases with
643 Translational Read-Through-Inducing Drugs (TRIDs). *Biodrugs* **30**, 49-74 (2016).
- 644 5. K. M. Keeling, X. Xue, G. Gunn, D. M. Bedwell, Therapeutics Based on Stop Codon Readthrough. *Annu. Rev. Genom.*
645 *Hum. Genet.* **15**, 371-394 (2014).
- 646 6. M. Dabrowski, Z. Bukowy-Bieryllo, E. Zietkiewicz, Advances in therapeutic use of a drug-stimulated translational
647 readthrough of premature termination codons. *Mol. Med.* **24**, 25 (2018).
- 648 7. Welch, E.M., Barton, E.R., Zhuo, J., Tomizawa, Y., Friesen, W.J., Trifillis, P., Paushkin, S., Patel, M., Trotta, C.R., Hwang,
649 S. *et al.* (2007) PTC124 targets genetic disorders caused by nonsense mutations. *Nature*, **447**, 87-91.
- 650 8. Peltz, S.W., Morsy, M., Welch, E.M. and Jacobson, A. (2013) Ataluren as an agent for therapeutic nonsense suppression.
651 *Annu Rev Med*, **64**, 407-425.
- 652 9. A. Leier *et al.*, Mutation-Directed Therapeutics for Neurofibromatosis Type I. *Mol Ther Nucleic Acids* **20**, 739-753 (2020)
- 653 10. Lentini, L., Melfi, R., Di Leonardo, A., Spinello, A., Barone, G., Pace, A., Palumbo Piccionello, A. and Pibiri, I. (2014)
654 Toward a rationale for the PTC124 (Ataluren) promoted readthrough of premature stop codons: a computational approach
655 and GFP-reporter cell-based assay. *Mol Pharm*, **11**, 653-664.
- 656 11. Li, M., Andersson-Lendahl, M., Sejersen, T. and Arner, A. (2014) Muscle dysfunction and structural defects of
657 dystrophin-null sapje mutant zebrafish larvae are rescued by ataluren treatment. *FASEB J*, **28**, 1593-1599.
- 658 12. Bushby, K., Finkel, R., Wong, B., Barohn, R., Campbell, C., Comi, G.P., Connolly, A.M., Day, J.W., Flanigan, K.M.,
659 Goemans, N. *et al.* (2014) Ataluren treatment of patients with nonsense mutation dystrophinopathy. *Muscle Nerve*, **50**, 477-
660 487.
- 661 13. Drake, K.M., Dunmore, B.J., McNelly, L.N., Morrell, N.W. and Aldred, M.A. (2013) Correction of nonsense BMPR2
662 and SMAD9 mutations by ataluren in pulmonary arterial hypertension. *Am J Respir Cell Mol Biol*, **49**, 403-409.
- 663 14. Goldmann, T., Overlack, N., Wolfrum, U. and Nagel-Wolfrum, K. (2011) PTC124-mediated translational readthrough of
664 a nonsense mutation causing Usher syndrome type 1C. *Hum Gene Ther*, **22**, 537-547.
- 665 15. Gregory-Evans, C.Y., Wang, X., Wasan, K.M., Zhao, J., Metcalfe, A.L. and Gregory-Evans, K. (2014) Postnatal
666 manipulation of Pax6 dosage reverses congenital tissue malformation defects. *J Clin Invest*, **124**, 111-116.
- 667 16. Michorowska, S. Ataluren—Promising Therapeutic Premature Termination Codon Readthrough Frontrunner.
668 *Pharmaceuticals* 2021, **14**, 785.
- 669 17. M. Jospe-Kaufman, L. Siomin, M. Fridman, The relationship between the structure and toxicity of aminoglycoside
670 antibiotics. *Bioorg. Med. Chem. Lett.* **30**, 127218 (2020).
- 671 18. D. K. Crawford, I. Alroy, N. Sharpe, M. M. Goddeeris, G. Williams, ELX-02 Generates Protein via Premature Stop
672 Codon Read-Through without Inducing Native Stop Codon Read-Through Proteins. *J. Pharmacol. Exp. Ther.* **374**, 264-272
673 (2020).
- 674 19. Roy B, Leszyk JD, Mangus DA, Jacobson A. Nonsense suppression by near-cognate tRNAs employs alternative base
675 pairing at codon positions 1 and 3. *Proc Natl Acad Sci U S A*. 2015 Mar 10;112(10):3038-43.

- 676 20. Roy, B., Friesen, W.J., Tomizawa, Y., Leszyk, J.D., Zhuo, J., Johnson, B., Dakka, J., Trotta, C.R., Xue, X., Mutyam, V.
677 *et al.* (2016) Ataluren stimulates ribosomal selection of near-cognate tRNAs to promote nonsense suppression. *Proc Natl*
678 *Acad Sci U S A*, **113**, 12508-12513.
- 679 21. Ng, M.Y., Zhang, H., Weil, A., Singh, V., Jamiolkowski, R., Baradaran-Heravi, A., Roberge, M., Jacobson, A., Friesen,
680 W., Welch, E. *et al.* (2018) New in Vitro Assay Measuring Direct Interaction of Nonsense Suppressors with the Eukaryotic
681 Protein Synthesis Machinery. *ACS Med Chem Lett*, **9**, 1285-1291.
- 682 22. S. Inge-Vechtsov, G. Zhouravleva, M. Philippe, Eukaryotic release factors (eRFs) history. *Biol. Cell* 95, 195–209
683 (2003).
- 684 23. D. C. Soares, P. N. Barlow, H. J. Newbery, D. J. Porteous, C. M. Abbott, Structural models of human eEF1A1 and
685 eEF1A2 reveal two distinct surface clusters of sequence variation and potential differences in phosphorylation. *PLoS One* 4,
686 e6315 (2009).
- 687 24. R. Jørgensen, A. R. Merrill, G. R. Andersen, The life and death of translation elongation factor 2. *Biochem. Soc. Trans.*
688 **34**, 1–6 (2006).
- 689 25. R. J. Jackson, C. U. T. Hellen, T. V. Pestova, The mechanism of eukaryotic translation initiation and principles of its
690 regulation. *Nat. Rev. Mol. Cell Biol.* **11**, 113–127 (2010).
- 691 26. A. Ferguson *et al.*, Functional dynamics within the human ribosome regulate the rate of active protein synthesis. *Mol.*
692 *Cell* **60**, 475–486 (2015).
- 693 27. Ng, M.Y., Li, H., Ghelfi, M.D., Goldman, Y.E. and Cooperman, B.S. (2021) Ataluren and aminoglycosides stimulate
694 read-through of nonsense codons by orthogonal mechanisms. *Proc Natl Acad Sci U S A*, **118**:e2020599118.
- 695 28. Buchmueller KL, Hill BT, Platz MS, Weeks KM. RNA-tethered phenyl azide photocrosslinking via a short-lived
696 indiscriminant electrophile. *J Am Chem Soc.* 2003 Sep 10;125(36):10850-61.
- 697 29. Zinshteyn, B., Chan, D., England, W., Feng, C., Green, R. and Spitale, R.C. (2019) Assaying RNA structure with LASER-
698 Seq. *Nucleic Acids Res*, **47**, 43-55.
- 699 30. https://wiki.yeastgenome.org/index.php/Modified_Nucleotides_within_RNAs_in_S._cerevisiae Saccharomyces Genome
700 Database
- 701 31. Sharma S, Hartmann JD, Watzinger P, Klepper A, Peifer C, Kötter P, Lafontaine DLJ, Entian KD. A single N¹-
702 methyladenosine on the large ribosomal subunit rRNA impacts locally its structure and the translation of key metabolic
703 enzymes. *Sci Rep.* 2018 Aug 9;8(1):11904.
- 704 32. Taoka M, Nobe Y, Yamaki Y, Sato K, Ishikawa H, Izumikawa K, Yamauchi Y, Hirota K, Nakayama H, Takahashi N,
705 Isobe T. Landscape of the complete RNA chemical modifications in the human 80S ribosome. *Nucleic Acids Res.* 2018 Oct
706 12;46(18):9289-9298.
- 707 33. Zhirnov OV, Wollenzien P. Action spectra for UV-light induced RNA-RNA crosslinking in 16S ribosomal RNA in the
708 ribosome. *Photochem Photobiol Sci.* 2003 Jun;2(6):688-93.
- 709 34. Bhaskar, V., Graff-Meyer, A., Schenk, A.D., Cavadini, S., von Loeffelholz, O., Natchiar, S.K., Artus-Revel, C.G., Hotz,
710 H.R., Bretones, G., Klaholz, B.P. *et al.* (2020) Dynamics of uS19 C-Terminal Tail during the Translation Elongation Cycle
711 in Human Ribosomes. *Cell Rep*, **31**, 107473.
- 712 35. Shao S, Murray J, Brown A, Taunton J, Ramakrishnan V, Hegde RS. Decoding Mammalian Ribosome-mRNA States
713 by Translational GTPase Complexes. *Cell.* 2016 Nov 17;167(5):1229-1240.e15.
- 714 36. Shoemaker CJ, Green R. Kinetic analysis reveals the ordered coupling of translation termination and ribosome recycling
715 in yeast. *Proc Natl Acad Sci U S A.* 2011 Dec 20;108(51):E1392-8.
- 716 37. Lawson, M. R., Lessen, L. N., Wang, J., Prabhakar, A., Corsepius, N. C., Green, R., & Puglisi, J. D. (2021). Mechanisms
717 that ensure speed and fidelity in eukaryotic translation termination. *bioRxiv*. doi: <https://doi.org/10.1101/2021.04.01.438116>
- 718 38. Preis A, Heuer A, Barrio-Garcia C, Hauser A, Eyler DE, Berninghausen O, Green R, Becker T, Beckmann R. Cryoelectron
719 microscopic structures of eukaryotic translation termination complexes containing eRF1-eRF3 or eRF1-ABCE1. *Cell Rep.*
720 2014 Jul 10;8(1):59-65.

- 721 39. Susorov, D., Egri, S., & Korostelev, A. A. (2020). Termi-Luc: a versatile assay to monitor full-protein release from
722 ribosomes. *RNA*, 26(12), 2044-2050.
- 723 40. Hein MY, Hubner NC, Poser I, Cox J, Nagaraj N, Toyoda Y, Gak IA, Weisswange I, Mansfeld J, Buchholz F, Hyman
724 AA, Mann M. A human interactome in three quantitative dimensions organized by stoichiometries and abundances. *Cell*.
725 2015 163:712-23
- 726 41. Schuller AP, Green R. Roadblocks and resolutions in eukaryotic translation. *Nat Rev Mol Cell Biol*. 2018 Aug;19(8):526-
727 541.
- 728 42. B. Roy *et al.*, Ataluren Stimulates Ribosomal Selection of Near-Cognate tRNAs to Promote Nonsense Suppression. *Proc.*
729 *Natl. Acad. Sci. U. S. A.* **113**, 12508-12513 (2016).
- 730 43. S. W. Peltz, M. Morsy, E. M. Welch, A. Jacobson, Ataluren as an Agent for Therapeutic Nonsense Suppression. *Annu.*
731 *Rev. Med.* **64**, 407-425 (2013).
- 732 44. D. Kessel, A. Morgan, G. M. Garbo, Sites and efficacy of photodamage by tin etiopurpurin in vitro using different delivery
733 systems. *Photochem. Photobiol.* **54**, 193-196 (1991).
- 734 45. Crowley KS, Reinhart GD, Johnson AE. The signal sequence moves through a ribosomal tunnel into a noncytoplasmic
735 aqueous environment at the ER membrane early in translocation. *Cell*. 1993 73, 1101-15.
- 736 46. Zhang, H., Ng, M.Y., Chen, Y. and Cooperman, B.S. (2016) Kinetics of initiating polypeptide elongation in an IRES-
737 dependent system. *Elife*. 5:e13429.
- 738 47. Milon, P., Konevega, A. L., Peske, F., Fabbretti, A., Gualerzi, C. O., and Rodnina, M. V. Transient kinetics, fluorescence,
739 and FRET in studies of initiation of translation in bacteria (2007). *Methods Enzymol*, 430:1–30
- 740 48. Odom Jr, O. W., Robbins, D. J., Lynch, J., Dottavio-Martin, D., Kramer, G., & Hardesty, B. (1980). Distances between
741 3'ends of ribosomal ribonucleic acids reassembled into Escherichia coli ribosomes. *Biochemistry*, 19(26), 5947-5954.
- 742 49. Barhoom, S., Farrell, I., Shai, B., Dahary, D., Cooperman, B.S., Smilansky, Z., Elroy-Stein, O. and Ehrlich, M., 2013.
743 Dicodon monitoring of protein synthesis (DiCoMPS) reveals levels of synthesis of a viral protein in single cells. *Nucleic*
744 *acids research*, 41(18), pp.e177-e177.
- 745 50. Liu, J., Pampillo, M., Guo, F., Liu, S., Cooperman, B.S., Farrell, I., Dahary, D., Gan, B.S., O'Gorman, D.B., Smilansky,
746 Z. and Babwah, A.V., 2014. Monitoring collagen synthesis in fibroblasts using fluorescently labeled tRNA pairs. *Journal of*
747 *cellular physiology*, 229(9), pp.1121-1129.
- 748 51. McClary, B., Zinshteyn, B., Meyer, M., Jouanneau, M., Pellegrino, S., Yusupova, G., Schuller, A., Reyes, J.C.P., Lu, J.,
749 Guo, Z. *et al.* (2017) Inhibition of Eukaryotic Translation by the Antitumor Natural Product Agelastatin A. *Cell Chem Biol*,
750 **24**, 605-613 e605.
- 751 52. Busan S, Weeks KM. Accurate detection of chemical modifications in RNA by mutational profiling (MaP) with
752 ShapeMapper 2. *RNA*. 2018, 24(2):143-148
- 753 53. Dobin A, Davis CA, Schlesinger F, Drenkow J, Zaleski C, Jha S, Batut P, Chaisson M, Gingeras TR. (2013) STAR:
754 ultrafast universal RNA-seq aligner. *Bioinformatics*. 29:15-21.
- 755 54. Roy,R., Hohng,S. and Ha,T. (2008) A practical guide to single-molecule FRET. *Nat. Methods*, 5, 507–516.
- 756 55. Jamiolkowski, R. M., Chen, C., Cooperman, B. S., & Goldman, Y. E. (2017). tRNA fluctuations observed on stalled
757 ribosomes are suppressed during ongoing protein synthesis. *Biophysical journal*, 113(11), 2326-2335.
- 758 56. Flis, J., Holm, M., Rundlet, E. J., Loerke, J., Hilal, T., Dabrowski, M., Burger, J., Mielke, B., Blanchard, S.C., Spahn,
759 C.M.T .& Budkevich, T. V. (2018). tRNA translocation by the eukaryotic 80S ribosome and the impact of GTP
760 hydrolysis. *Cell reports*, 25(10), 2676-2688.37.
- 761 57. Chen, C.; Stevens, B.; Kaur, J.; Cabral, D.; Liu, H.; Wang, Y.; Zhang, H.; Rosenblum, G.; Smilansky, Z.; Goldman, Y.
762 E.; et al. Single-Molecule Fluorescence Measurements of Ribosomal Translocation Dynamics. *Mol. Cell* 2011, 42, 367–377.
- 763 58. Bevington, P.R., and Robinson, D.K. (2002). *Data Reduction and Error Analysis for the Physical Sciences* (New York:
764 McGraw- Hill).

765 59. Woody, M.S., Lewis, J.H., Greenberg, M.J., Goldman, Y.E., and Ostap, E.M. (2016). MEMLET: An Easy-to-Use Tool
766 for Data Fitting and Model Comparison Using Maximum-Likelihood Estimation. *Biophys. J.* *111*, 273–282.

767
768 **ACKNOWLEDGEMENTS**

769 We gratefully acknowledge many helpful discussions with Boris Zynshyeyn on the use of RNA-Seq, and gifts of GJ072,
770 ataluren sodium salt and 3-[5-(4-azidophenyl)-1,2,4-oxadiazol-3-yl]-6-iodo benzoic acid from PTC Therapeutics and of the
771 eERF1 and eRF3 plasmids from Allan Jacobson. This work was supported by research grants to B.S.C. (PTC Therapeutics;
772 Cystic Fibrosis Foundation-COOPER21G0; and NIH GM127374), to Y.E.G. (NIH GM118139), and to DMC (NIH
773 GM118510).

774
775 **Author Contributions Statement:** SH was responsible for planning, executing, and interpreting the results of the
776 photoaffinity labeling experiments; AB and CF were responsible for planning, executing, and interpreting the results of the
777 single molecule experiments; MDG was responsible for the preparation of Atto 647- ϵ -lysine tRNA^{Lys} and for planning,
778 executing, and interpreting the results of the plate reader anisotropy and Millipore filtration assays; HL was responsible for
779 the preparation and characterization of ribosomes, tRNAs, CrPV-IRES-mRNA, and both elongation and termination,
780 factors, DMC made valuable suggestions for the conduct of the RNA-Seq experiments and provided financial support, YEG
781 was responsible for overseeing the single molecule experiments, writing the manuscript, and providing financial support,
782 BSC was responsible for overseeing the photoaffinity labeling, plate reader anisotropy and Millipore filtration
783 experiments, writing the manuscript, and providing financial support.

784
785 **Competing Interests Statement.** The authors declare no competing interests.

786
787

788
789
790

TABLES

Table 1. Photoincorporation yields (mole%) into RNase H Fragments ^a						
Target	Experiment	Competing Ligand ^b	Mutated site(s)/RNase Fragment			
			18S A1195/ I: 18S 1151 - 1206	26S-A3093/ II: 26S 3069 - 3113	26S- A2669;A2672/ III: 26S 2638 - 2702	CrPV-IRES U177;G186 IV: 156-221
Stop- POST5	PAL, 300 μM AzAt	-	<i>1.55 ± 0.20</i>	0.40 ± 0.01	1.07 ± 0.14	3.2 ± 0.8
		eRF1/eRF3/ GDPNP	0.07 ± 0.03	0.18 ± 0.10	0.19 ± 0.02	2.9 ± 0.6
		eRF1	0.19 ± 0.07	0.18 ± 0.01	0.20 ± 0.01	-
	PAL, 30 μM AzAt	-	0.26 ± 0.03	0.03 ± 0.01	0.13 ± 0.04	-
		Ataluren, 500 μM	0.06 ± 0.01	0.06 ± 0.01	0.10 ± 0.04	-
		GJ072, 150 μM	0.10 ± 0.01	0.07 ± 0.01	0.07 ± 0.01	-
PRE, 300 μM AzAt	-	0.012 ± 0.003	0.04 ± 0.01	0.03 ± 0.02	-	
80S- IRES	PAL, 300 μM AzAt	-	<i>1.03 ± 0.33</i>	<i>0.50 ± 0.09</i>	<i>1.01 ± 0.12</i>	-
		eRF1/eRF3/ GDPNP	0.56 ± 0.06	<i>0.55 ± 0.12</i>	<i>0.94 ± 0.23</i>	-

^a Error ranges are ± average deviations, n=2 or 3 (italicized) independent determinations; ^b Added concentrations: eRF1, 2 μM; eRF3, 4 μM; GDPNP, 1 mM

791
792

Table 2. Sites of fluorophore incorporation within fluorescent Stop-POST5 complexes			
Stop-POST5	Lys within FKVRN	tRNA ^{Gln}	Ribosome ^a
Atto(pep)	Atto647	unlabeled	unlabeled
Atto(pep)-Cy(tRNA)	Atto647	Cy3	unlabeled
Atto(rbsm)-Cy(tRNA)	unlabeled	Cy3	Atto647N
Atto(pep)-Cy(rbsm)	Atto647	unlabeled	Cy3

^a ribosomes were labeled to a total stoichiometry of ~ 1/ribosome spread over Lys residues within r-proteins

793
794
795
796

FIGURE LEGENDS

Figure 1. a. Structures of ataluren and [³H]-AzAt. T refers to tritium. N₃ is the azide which confers photolability on azidoataluren. **b.** Stop-IRES mRNA encoding FKVRQStopLM. The cartoon depicts the Stop-POST5 complex containing FKVRQ-tRNA^{Gln} bound in the P-site adjacent to an empty A-site containing the UGA stop codon, and the incoming eRF1.eRF3.GTP complex which catalyzes cleavage of the ester bond linking FKVRQ to tRNA^{Gln} after binding to the A-site.

Figure 2. AzAt Photoaffinity Labeling. a. AzAt photoincorporation into Stop-POST5, the RNA fraction of Stop-POST5, 80S.IRES, and the RNA fraction of 80S.IRES. All of the labeling stoichiometries are normalized to that of Stop-POST5 at 600 μM AzAt, which was equal to 1.2/Stop-POST5. **b.** AzAt photoincorporation into eRF1 both alone and complexed with eRF3.GDPNP. The values are normalized to the saturation labeling of isolated eRF1. **c.** Inhibition of AzAt (250 μM) photoincorporation by the addition of either ataluren (1,000 μM) or GJ072 (150 μM). **d.** The mutation rate fold change for PAL vs. PRE samples for Stop-POST5 (red) and 80S.IRES complexes (blue) for the 22 sites most pertinent for ataluren function, and the asterisks indicates sites of particular interest (see text). **e.** Saturation curves for photoincorporation into 18S-A1195, as measured by photoincorporation into Fragment I, vs. the sum of the photoincorporations into 26S A3093, A2669, and A2672, as measured by photoincorporation into Fragments II and III. **f.** Location of A1195 within the 40S subunit containing bound eRF1. **g.** Locations of A2669, A2672, and A3093 within the 60S subunit containing bound eRF1. All of the error bars in this Figure represent average deviations for n=2 independent determinations, with the exception of the eRF1 labeling within the ternary complex in b, for which n=3. Source data for **a – e** are provided as a Source Data file.

Figure 3. Typical traces showing the dissociation of Atto-647 labeled peptide (red) and Cy3-labeled tRNA (green) following eRF1/eRF3 injection. In the time-lapse experiment the sample was briefly illuminated between fixed time intervals. **a.** and **c.** Sample traces following eRF1/eRF3 injection. In **a** the peptide signal disappears prior to tRNA signal; in **c** the tRNA signal disappears prior to peptide signal. **b.** and **d.** Corresponding real-time scatter plots of the traces presented in **a** and **c**, where each dot represents one frame. **e.** Sample trace from a control experiment where only buffer was injected to obtain the photobleaching/spontaneous dissociation rate, which is clearly much slower than the rates seen in **a** and **c**. **f.** The real-time scatter plot of the trace presented in **e**. Source data for **a**, **c**, and **e** are provided as a Source Data file.

Figure 4. a. and **b.** Cumulative distributions of **a.** peptide and **b.** tRNA dissociation times at indicated RFC concentrations, one also with 1 mM ataluren. Each cumulative distribution is constructed from ≥300 kinetic traces. **c.** and **d.** Rates of dissociation of **c.** peptide and **d.** tRNA as a function of RFC concentration at different fixed ataluren concentrations. Error bars are ± s.e.m. for n = 250- 750 trials. **e.** and **f.** Normalized plots of ensemble experiments showing single exponential fits (solid lines) of decimated smoothed raw data (points) of atto647 pentapeptide release reaction measured by fluorescence anisotropy decay vs. time at 25 °C. **e.** At indicated RFC concentrations. The control shows the near constancy of observed anisotropy in the absence of added RFC or ataluren. **f.** At an RFC concentration of 0.0625 μM and varying ataluren concentrations. **g.** The rates of dissociation of atto647 pentapeptide in ensemble experiments as a function of free RFC concentration at varying ataluren concentrations. Error bars are average deviation (a. d.) for n= 2 – 6 independent determinations. Values of n for each point are presented in Supplementary Table S5. **h.** Ataluren inhibition of normalized rates of dissociation of atto647 pentapeptide as measured by single molecule (red) and plate reader (black) assays. [eRF1], 32 nM; [eRF3], 0.2 μM and 0.8 μM in the single molecule and ensemble assays, respectively. Error bars are ± s.e.m. n ≥ 250 trials (single molecule) and ± a.d., n=2 independent determinations (plate reader). **i.** Rates of dissociation of atto647 labeled and unlabeled pentapeptide as measured by millipore filtration, calculated using both filtrate and filter retained values. Error bars are ± s.d., n= 8 independent measurements for all points except for the 4 minute measurements, for which n = 11. [eRF1], 0.2 μM; [eRF3], 0.8 μM; POST5, 0.05 μM. **j.** Ataluren inhibition of peptide and tRNA release when added at different times (4 - 25s) following RFC addition to Stop-POST5. [RFC], 0.08μM; [Ataluren], 1 mM. Values at zero-time correspond to simultaneous addition of ataluren and RFC. Error bars are ± s.e.m. for n ≥ 200 trials. Source data for all panels are provided as a Source Data file.

Figure 5. Scatter plots of peptide and tRNA dissociation times. Each point represents dissociation times from an individual ribosome. CC is correlation coefficient. **a.** 2 μM RFC. **b.** 16 nM RFC. Source data are provided as a Source Data file.

Figure 6. A simplified model for RFC catalysis of termination. This model, consistent with all of our results, as well as with recent published results of others (30), posits that ataluren inhibition results from the cooperative binding of *n* molecules of ataluren to the pretermination complex P5 in competition with RFC binding. It also invokes a hypothetical

853 complex C3 resulting from an at least partial rate-determining conformational change, following cleavage of the tRNA-
854 peptide ester bond to account for the similarity in the rate constants of tRNA, peptide, and eRF1 release (see text). The
855 question marks associated with possible eRF1 release are shown to indicate our current uncertainty as to whether eRF1
856 release is coordinated with either peptide or tRNA release, or proceeds independently of either.

Supplementary Files

This is a list of supplementary files associated with this preprint. Click to download.

- [Table1SourceData.xlsx](#)
- [SupplementaryData1.xlsx](#)
- [SupplementaryFigures1246c11SourceData.xlsx](#)
- [SupplementaryTable1SourceData.xlsx](#)
- [HuangSupplementaryInformation.pdf](#)